Cell cycle-resolved Hi-C reveals unexpected plasticity of A/B compartments across interphase

Linda Choubani[1,2], Hisashi Miura[1], Takako Ichinose[1], Asami Oji[1], Rory T. Cerbus[1], Ichiro Hiratani[1]*

[1]Laboratory for Developmental Epigenetics, RIKEN Center for Biosystems Dynamics Research (BDR); Kobe, Japan.

[2]Department of Developmental Biology and Regenerative Medicine, Division of Physiology and Cell Biology, Graduate School of Medicine, Kobe University, Kobe, Japan.

*Corresponding author. Email: ichiro.hiratani@riken.jp

Abstract

The spatial organization of chromatin into active (A) and inactive (B) nuclear compartments is fundamental to genome regulation, yet their cell-cycle dynamics remain largely unexplored. Most research on chromatin dynamics during the cell cycle has primarily focused on events surrounding mitosis, providing only limited insight into chromatin behavior during S-phase. To address this gap, we developed a simple, drug-free approach that combines the Fucci cell-cycle indicator with *in situ* Hi-C to comprehensively analyze A/B compartment dynamics throughout interphase in mouse embryonic stem cells (mESCs). Unexpectedly, and contrary to prevailing views, we found that A/B compartment strength increased abruptly upon S-phase entry, stabilized during S-phase, and subsequently declined in late S/G2. This abrupt strengthening, which we termed 'compartment maturation,' required passage through the G1/S transition but was independent of active DNA synthesis. This maturation involved substantial architectural remodeling, particularly within the A compartment, which consolidated into a more organized structure as individual A domains rearranged to form long-range interactions. Moreover, compartment maturation was not limited to mESCs but was also observed across different developmental contexts in mice. Based on these observations, we propose a revised, stepwise model of nuclear compartmentalization during cell-cycle progression, consisting of four distinct stages: chromosome unfolding (G1), chromatin maturation (G1/S), stabilization (S phase), and refolding (G2). These findings reveal the unexpected plasticity of A/B compartments and underscore the G1/S transition as a critical period for their reorganization.

Introduction

The three-dimensional (3D) organization of the genome within the nucleus plays a fundamental role in regulating essential cellular processes, including gene expression, DNA replication, and repair[1,2]. High-throughput chromosome conformation capture (Hi-C) techniques[3] have revolutionized our ability to probe this organization, revealing the existence of megabase (Mb)-scale chromosomal compartments in interphase cells. These appear as a characteristic plaid pattern on Hi-C contact maps, reflecting the segregation of chromatin into self-interacting active (A) and inactive (B) nuclear compartments[3]. This pattern is identified computationally through principal component analysis (PCA) of the Hi-C contact matrix, where the first principal component (PC1) serves as a quantitative eigenvector; genomic bins are assigned to A (positive PC1 values) or B (negative PC1 values) compartments based on their correlated interaction profiles[3]. Broadly speaking, A and B compartments correspond to euchromatin and heterochromatin, typically located in the nuclear interior and at the nuclear periphery, respectively[4].

Despite their fundamental significance in genome function, the principles governing compartment formation remain largely elusive. Over the past decade, researchers have increasingly focused on the cell cycle regulation to unravel the principles of chromatin organization, given that compartments are largely lost during mitosis and re-established during interphase[5]. This process begins as chromosomes compact into their distinct, rod-like shapes during prophase[6,7]. Following mitosis, as cells traverse the M/G1 transition, chromosomes expand from this highly condensed state and gradually unfold to re-establish interphase chromatin architecture. Time-course Hi-C studies of this critical window[8–11] supported a "compartment expansion" model, positing that compartment boundaries are established soon after mitotic exit, followed by a gradual strengthening of chromatin interactions and their simultaneous expansion outward from the diagonal on Hi-C contact maps, reflecting the progressive increase in long-range interactions during G1. This progression culminates in the model proposed in the pioneering study by Nagano *et al.*[12], where compartmentalization progressively strengthens after mitotic exit, peaking in G2 just before its rapid collapse in the subsequent mitosis.

Despite these insights, significant gaps remain in our knowledge. Although compartments were among the first structures identified in Hi-C maps, they have often not been the primary focus of studies and are frequently treated as binary, static entities. Even when they have been investigated, the emphasis has typically been placed on Hi-C PC1-defined compartment boundaries rather than on the internal dynamics of the compartments themselves. Furthermore, variability in compartment calculation methods across studies complicates direct comparisons and hampers a comprehensive understanding. Importantly, while previous studies have illuminated events around mitosis, they have left the S-phase notably underexplored. This is a critical gap given the strong correlation between A/B compartments and DNA replication timing, whereby A regions replicate in early S-phase and B regions in late S-phase[13,14]. The fragmented nature of the existing cell-cycle Hi-C datasets is further complicated by the reliance on synchronization drugs in most studies, which can introduce population heterogeneity and confound biological interpretation[15].

In this study, we address these challenges by thoroughly investigating the temporal dynamics of interphase A/B compartments, with a special emphasis on the G1-to-S transition, a crucial yet understudied period for the coordinated establishment of 3D genome structure and DNA replication.

Results

Drug-free cell cycle-phasing system in mESCs

To investigate how A/B nuclear compartments change throughout the cell cycle, we established a drug-free synchronization approach in mouse embryonic stem cells (mESCs) to avoid the heterogeneity associated with the use of chemical inhibitors. For high-resolution cell-cycle discrimination, we used the Fucci (SA) mESC line[16,17], which expresses Cdt1-mCherry in G1 (degraded at the G1/S transition) and Geminin-mVenus in S/G2/M (accumulating from S-phase entry onwards) (**Fig. 1A).** The reciprocal fluorescence patterns of Cdt1 and Geminin enabled distinct and dynamic visualization of cell cycle phases, thereby allowing accurate sorting of highly pure cell populations for Hi-C without relying on chemical synchronization.

To confirm the suitability of the Fucci markers for this purpose, we performed imaging and fluorescence-activated cell sorting (FACS) analysis following EdU staining, which labels S-phase cells (**Fig. S1A**)**.** As expected, EdU incorporation correlated with Geminin signal accumulation and Cdt1 signal depletion **(Fig. S1B,C)**.

To monitor cell-cycle progression of individual cells, we conducted time-lapse imaging over a 50-hour period, capturing images every 10 minutes using Differential Interference Contrast (DIC), mCherry (Cdt1), and mVenus (Geminin) fluorescence **(Fig. S2A).** We manually tracked individual cells and included only those that completed a full cell cycle from one mitosis to the next for quantitative analysis **(Fig. S2B)**. Our analysis revealed minimal variation in overall cell-cycle length among cells (**Fig. S2C**). We also quantified the duration of the G1 phase for each cell, which we defined as the time from mitosis until mCherry fluorescence reached its peak. The remaining time was defined as the duration of the S/G2/M phase. The G1 phase lasted approximately 1.5 hours (**Fig. S2D**), consistent with the known characteristically short G1 phase of mESCs[18], with relatively small cell-to-cell variability **(Fig. S2B,D)**.

The above results confirmed that Fucci markers could reliably delineate cell-cycle phases, allowing us to sort homogeneous populations by FACS for subsequent Hi-C analysis. To achieve this, asynchronously growing cells were first fixed, permeabilized, and stained for DNA before being subjected to FACS (**Fig. 1A**). S-phase cells (subdivided into early, mid, and late S, each representing approximately 3-hour time windows, assuming a 10-hour S-phase) and G2-phase cells were sorted based on DNA content (**Fig. 1B**). For G1 cells, we employed a sequential gating strategy using both Fucci markers and DNA content (**Fig. 1C**). The population was first gated to include only Geminin-negative cells, followed by a second gate selecting only cells with a 2C DNA content. From this refined G1 population, we further sorted early, mid, and late G1 fractions based on ascending mCherry fluorescence intensity, with each fraction comprising approximately 30% of the population to achieve sub-hour temporal resolution. Finally, the sorted cells (0.5–1 million cells per fraction) were subjected to in situ Hi-C (**Fig. 1D**).

Stepwise changes in higher-order chromatin organization during interphase

Hi-C biological replicates were highly concordant (**Fig. S3A,B**). Consistent with previous studies, we observed a continuum of cis-interactions throughout interphase, as shown by contact decay profiles[12] (**Fig. 1E**). Cis-compartment structure and boundaries (Hi-C PC1) were already distinguishable from early G1 (**Fig. 1G, Fig. S3C**), albeit with a low PC1 contribution rate at this stage (**Fig. S3D**). Furthermore, Hi-C interaction maps (**Fig. 1G, Fig. S4A**) revealed that long-range chromatin interactions formed gradually from early G1 to late G1, expanding away from the diagonal on the map, as previously described in M-to-G1 time-course Hi-C studies[8,9,11].

Interestingly, however, this expansion from the diagonal culminated in late G1, when interactions spanning the farthest genomic distances (i.e., the regions most distant from the diagonal) were most pronounced (**Fig. 1G, Fig. S4A**). This trend was also evident in the contact decay profiles (**Fig. 1E**) and contact probability plots (**Fig. 1F, Fig. S4B**), which showed the greatest enrichment for contacts > 50 Mb in late G1. As cells entered S-phase, the Hi-C plaid pattern showed a distinct increase in sharpness, which subsequently became progressively blurred during late S-phase and further in G2. Notably, G2 cells displayed a thickened signal along the Hi-C map diagonal (**Fig. 1G, Fig. S4A**), a chromatin organization reminiscent of mitotic chromosomes[5,6]. This finding suggests that the onset of mitotic chromosome condensation may occur earlier than previously thought, during G2 phase (as discussed further below).

While a previous study has linked DNA replication to stronger compartmentalization[12], we found that the change in compartment strength was strikingly abrupt during the late G1 to early-S transition, as revealed by saddle plots, which quantify Hi-C contact enrichment between genomic bins ranked by their PC1 values (**Fig. 1H,I**). This shift, which we refer to as 'compartment maturation', was accompanied by a notable depletion of A-B interactions and an enrichment of A-A interactions (**Fig. 1H**). Compartment strength then stabilized during S phase, which constitutes the longest phase of the mESC cell cycle (**Fig. S1C**, > 60% cells in S-phase by FACS). Subsequently, a decrease in compartment strength began in late S, followed by an even more significant decrease in G2 (**Fig. 1H,I**). This mirrored the observation from the Hi-C maps mentioned earlier (**Fig. 1G, Fig. S4A**).

The observed decrease in compartment strength during G2 contrasted with a previous report by Nagano *et al.*[12], which showed maximal compartmentalization in G2. However, it should be noted that a unique compartment identification method was employed in that single-cell Hi-C study[12], distinct from the standard *de novo* compartment calling approach used in most Hi-C studies (see **Supplementary Note** for details). Therefore, we attribute this discrepancy not to differences in biological samples or chromatin conformation capture technologies, but rather to technical or interpretative differences arising from the distinct A/B compartment identification methods used. To further support this conclusion, we reanalyzed the cell cycle-phased pooled single-cell Hi-C data from Nagano *et al.*[12] using the conventional compartment-calling method and observed a trend consistent with our findings (**Fig. S5**), with compartment strength being maximal in early/mid S and decreasing in late S/G2. Thus, our analysis reconciles the apparent discrepancy with Nagano *et al.*[12] and supports a revised model in which compartment strength peaks in early S-phase and subsequently weakens toward G2, rather than continuously strengthening throughout interphase.

Notably, the pooled single-cell Hi-C data from Nagano *et al.*[12] showed a clear diagonal thickening in late S/G2 cells (**Fig. S5C**), in agreement with our observations above (**Fig. 1G, Fig. S4A**). Taken together, these data suggest that the structural transition toward mitotic chromosomes may already be initiated in late G2, a view further supported by a live-cell imaging study of interphase-to-mitosis chromosome dynamics showing prophase-like chromosome axis prealignment during G2[19].

Compartment maturation requires S-phase entry but is independent of active DNA synthesis

Intrigued by the abrupt and pronounced compartmentalization shift, or compartment maturation, observed during the short transition from late G1 to early S, we investigated its relationship to DNA replication. Specifically, we asked whether the G1-to-S transition was the direct cause of compartment maturation, or whether the shift in compartmentalization reflects an intrinsic chromatin program that proceeds independently of cell-cycle stage. To test this, we designed two distinct cell-cycle perturbation

experiments to induce prolonged arrest at two critical points, either just before or at the start of S-phase, and assessed their effects on compartment architecture.

Our first experimental perturbation aimed to determine whether prolonged G1-arrest, preventing S-phase entry altogether, would influence compartment maturation. Preventing S-phase entry in mESCs is particularly challenging; however, we found that the mTOR inhibitor INK-128 induces a reversible G1-like arrest in mESCs at a concentration of 1 µM (**Fig. S6**). Cells were treated with INK-128 for 24, 72, and 120 hours (**Fig. 2A**). FACS analysis confirmed that cells remained arrested at a 2C DNA content at all timepoints. Concurrently, they exhibited a Geminin-negative state, while maintaining high levels of Cdt1, features characteristic of late G1 cells (**Fig. S7A**). To minimize technical artifacts arising from copy-number differences, cells with a 2C DNA content were sorted at all three timepoints prior to performing Hi-C (**Fig. 2A, Fig. S7A**).

Hi-C contact maps from INK-128-treated cells (**Fig. 2B**) resembled a late G1-like chromatin organization (**Fig. 1G**). Saddle plot profiles (**Fig. 2C**) similarly showed compartment strength comparable to that of late G1 (**Fig. 1H**). Although INK-128-treated cells displayed a slightly higher degree of compartment segregation (**Fig. 2C**) and increased long-range interaction formation relative to typical late G1 cells (**Fig. S7B**), the characteristic upward shift in compartment segregation and the enrichment of A-A interactions, indicative of compartment maturation, were notably absent.

The second experiment examined the effect of prolonged G1/S arrest on chromatin compartments. mESCs were first arrested at metaphase using Nocodazole and then released into medium containing a high concentration of Thymidine. Cells were subsequently collected at 3-hour intervals post-release (3, 6, 9, and 12 hours) (**Fig. 2D**). FACS profiles (**Fig. S7C**) confirmed the accumulation of cells with a 2C DNA content following release from Nocodazole arrest. Approximately 6 hours after release, cells began to enter S-phase, as indicated by their transition from a Cdt1-positive/Geminin-negative (Cdt1+Geminin–) to a Cdt1-negative/Geminin-positive (Cdt1–Geminin+) state (**Fig. S7C**). This S-phase fraction progressively increased, leading to an almost complete conversion of 2C DNA content cells to the Cdt1–Geminin+ state after 12 hours of Thymidine treatment, with virtually no remaining G1 (Cdt1+Geminin–) cells. These results confirm that the cell population was successfully synchronized at the G1/S boundary, representing a pre-replicative state where replication had not yet initiated, although cell-cycle markers indicated entry into S-phase.

As in the previous time-course experiment, cells collected at all timepoints were FACS-sorted based on their 2C DNA content prior to performing Hi-C **(Fig. 2D, Fig. S7C)**. Hi-C analysis of these samples revealed the emergence of a distinct plaid pattern as early as 3 hours post-release from Nocodazole (**Fig. 2E**), with compartment strength (**Fig. 2F**) comparable to that of late G1 (**Fig. 1G,H**). Strikingly, despite sharing the same 2C DNA content, compartment strength continued to increase over time, as evidenced by the progressive sharpening of the Hi-C plaid pattern (**Fig. 2E**) and by saddle plot analysis (**Fig. 2F**). By 9 and 12 hours of Thymidine treatment, A/B compartment strength had reached levels similar to those of normal early- to mid-S cells (**Fig. 1G,H**). Furthermore, contact probability plots comparing late G1 and Thymidine-treated cells (**Fig. S7D**) revealed an 'S-like' trajectory, characterized by a decrease in long-range interactions relative to late G1.

Principal Component Analysis (PCA) of the Thymidine- and INK-128-treated Hi-C matrices, alongside those from normal cell-cycle phases, further clarified these findings (**Fig. 2G**). Specifically, INK-128-treated samples clustered closely with late G1, whereas Thymidine-treated cells aligned closely with the S-phase trajectory, particularly along the PC1 axis, which accounted for 78% of the total variation. Additionally, t-distributed stochastic neighbor embedding (t-SNE) followed by k-means clustering (k=2) of saddle plot data (**Fig. S7E**) revealed a clear separation between INK-128 and Thymidine samples.

Thymidine-treated cells—with the exception of the 'THY_3H' sample, which largely represented G1 cells—clustered with S-phase samples (thus S-like), whereas INK-128-treated cells grouped with G1 (thus G1-like).

Collectively, our results demonstrate that maturation of nuclear A/B compartments is a direct consequence of S-phase entry, and that this structural reorganization occurs independently of active DNA synthesis.

Formation of a consolidated A compartment in S-phase

To characterize compartment maturation in greater detail, we performed subcompartment analysis using the Calder2 tool[20]. This computational framework integrates information from multiple principal components of the Hi-C contact matrix to classify genome structures into eight distinct types based on their multi-dimensional interaction signatures. The resulting subcompartments, ranked from 0.125 (strongest B) to 1 (strongest A), provide a finer resolution view of the organization within global A/B compartments. Given the high concordance of our cell-cycle-phased Hi-C biological replicates, we merged them for all downstream analyses.

Visual inspection of subcompartment profiles for individual chromosomes at 40-kb resolution (**Fig. 3A, Fig. S8**) revealed that, from early S-phase onward, minor variations among A subcompartment domains were largely lost and replaced by more homogeneous, predominantly strong A (dark red) domains. Quantification of genomic bins assigned to each subcompartment type (**Fig. 3B**) revealed a striking and progressive accumulation of strong A subcompartment genomic bins (rank 1) from early G1, peaking in mid S-phase and decreasing thereafter in late S and G2. Concurrently, weak A and B bins were reduced from early G1 to mid S, suggesting a transition of subcompartments towards stronger A states. Consistent with this, comparison of the average sizes of different subcompartment domains between late G1 and early S (**Fig. 3C**) revealed that only A subcompartment domains increased significantly in size, with the most statistically significant change observed in strong A subcompartment domains (ranks 0.875 and 1).

We also observed a "smoother" appearance in A-compartment profiles (Hi-C PC1 > 0) in S-phase cells, characterized by fewer signal spikes (example shown in **Fig. S9A**). To quantify this trend, we calculated the mean-square gradient (MSG), defined as the average of the squared difference between adjacent signal values (see Methods). A larger MSG value reflects a more irregular (spiky) compartment signal, whereas a lower value indicates a smoother signal (**Fig. S9B**). By measuring the MSG ratio between strong A versus B compartments, we found that in early G1, the A-compartment signal was more than twice as irregular as the B-compartment signal. However, upon S-phase entry and throughout cell-cycle progression, this ratio steadily declined, and by late S and G2, the two signals had converged to a similar degree of smoothness (**Fig. S9C**). When comparing the average MSG of the strongest A and B compartment regions (**Fig. S9D**), we observed no consistent trend for the B compartment. In contrast, the A compartment signal progressively became smoother, reaching maximal smoothness (lowest MSG value) in mid-S, followed by an increase in late S and G2.

These results reveal a previously unrecognized feature of chromatin organization during S-phase progression, whereby the A compartment becomes highly dynamic and reorganizes into a more uniform, consolidated strong A compartment. We refer to this process as "A-compartment consolidation."

A-compartment consolidation is a robust feature across developmental contexts

mESCs possess a unique nuclear architecture characterized by more open and decondensed chromatin, presenting fewer and more dispersed heterochromatin foci[21] and a generally less compartmentalized 3D genome compared with their differentiated counterparts[22]. This distinctive organization prompted us to ask whether the S-phase-associated A-compartment consolidation observed in mESCs is a unique feature of pluripotent cells or represents a more broadly conserved phenomenon across other cell types.

To address this question, we utilized the single-cell HiRES (Hi-C and RNA-seq employed simultaneously) dataset from Liu *et al.*[23], which provides comprehensive single-cell Hi-C and RNA-seq data across a wide range of cell types, developmental stages, and cell-cycle phases. Although the accompanying metadata include extensive annotations for individual cells, identifying specific cell types at defined developmental stages and cell-cycle phases with sufficient read coverage for robust population-level analysis proved challenging. We therefore focused our analysis on four distinct cell types spanning three developmental stages—neural ectoderm (E7.5), neural tube (E8.5), mixed late mesenchyme (E10.5), and extra-embryonic (ExE) endoderm (E7.5) (**Fig. 4A**)—that provided sufficient Hi-C read coverage for both G1 and mid-S phase populations (see **Table S1**). This selection captured a developmental continuum extending beyond the stage equivalent to mESCs, which corresponds approximately to E4.5[24]. We then performed pseudo-bulk Hi-C analysis by aggregating Hi-C reads from individual cells, grouped by cell-cycle phase (G1 and mid-S) within each selected cell type and developmental stage.

In all four cell types, we observed the characteristic increase in compartment strength (maturation) previously seen in mESCs when comparing late G1 and mid-S cells. Furthermore, we detected the hallmark increase in A-A interactions during the G1-to-mid-S transition, even in cell types where B-B interactions were more prominent than A-A interactions in G1, such as mixed late mesenchyme (E10.5) (**Fig. 4B**).

Calder subcompartment analysis of all four cell types at 200-kb resolution (**Fig. 4C**) mirrored the trend observed in mESCs, showing an enrichment of strong A (rank 1) subcompartment bins and a corresponding reduction in weak subcompartment bins in mid-S cells. Together, these findings strongly indicate that compartment maturation and the accompanying A-compartment consolidation represent a robust and universally observed feature across different developmental contexts.

A-compartment consolidation during S-phase involves enhanced long-range contacts and structural reorganization

To further characterize A-compartment consolidation, we performed a distance-based compartment strength analysis using the Pentad tool[25]. Specifically, we quantified interactions within A (A-A), within B (B-B), and between A and B (A-B) compartments across four genomic distance ranges: short-range (1–10 Mb), mid-range (10–25 Mb), mid/long-range (25–50 Mb) and long-range (> 50 Mb) throughout interphase (**Fig. 5A**). As expected, positive interaction frequencies were observed for A-A and B-B pairs, and negative frequencies for A-B pairs, at all stages. More notably, our analysis revealed a marked enrichment of long-range A-A interactions emerging in early S-phase, which was substantially reduced in G2. Concurrently, we observed a depletion of short- and mid-range A-B interactions in early S-phase that persisted through mid-S, followed by a slight increase in late-S and a more pronounced increase in G2. In contrast, interactions showed minimal change across all distances throughout interphase.

By measuring intra-compartment (intra-A and intra-B; i.e., short-range A-A and B-B) and inter-compartment (inter-A and inter-B; i.e., long-range A-A and B-B) interaction strengths (**Fig. 5B**), we found that all interaction types followed a general "rise-and-fall" trend, similar to that observed in non-distance-based saddle plots (**Fig. 1H,I**), with the most pronounced and statistically significant changes occurring

from late G1 to early S. Most notably, inter-A interaction strength exhibited the largest and most statistically significant increase during this transition ($P = 1.74 \times 10^{-1}$, Δ median = 0.64) (**Fig. 5B,C**), corroborating our observation of enriched long-range A-A interactions during S-phase (**Fig. 5A**). These observations point to large-scale rearrangements within A-compartment regions as a potential driver of the global shift in A/B compartment segregation at the G1/S transition.

To further investigate this, we visually inspected Hi-C contact maps of A-compartment domains from late G1 and early S-phase. This revealed a striking pattern of spatial reorganization in large A domains, characterized by a sharp reduction in interactions between A-compartment boundaries and their internal regions (**Fig. 5D**, purple dotted circles). Most notably, these large A domains became selectively inaccessible to neighboring smaller A domains, with only boundary-associated interactions persisting (**Fig. 5D**, black rectangles). The recurrence of this pattern across multiple domains (**Fig. S10**) suggested a non-random spatial reorganization specific to S phase. We hypothesize that this reorganization process reflects the formation of "peninsula-like" structures (**Fig. 5E**), in which internal A regions extend outward while remaining tethered at their bases (**Fig. 5E**).

3D modeling reveals the structural basis of cell cycle-dependent A/B compartment dynamics

To obtain a structural perspective on the proposed "peninsula-like" formations, we performed quantitative 3D modeling of chromosomes across all sampled interphase stages using LorDG, a deterministic genome modeler within the GenomeFlow pipeline that generates reproducible polymer-like 3D structures from Hi-C data[26]. Analysis of merged biological replicates at 200-kb resolution with optimized parameters (conversion factor = 0.6, max iterations = 10,000) yielded models that closely matched the experimental Hi-C data, with an average absolute Spearman correlation of 0.77 (**Fig. S11**).

Visually, the simulations with overlaid A/B compartment tracks at the same resolution (e.g., chromosomes 2 and 17 in **Fig. 6A**) faithfully recapitulated the transition from rod-like early G1 chromosomes to a more interphase-like organization in late G1, and most importantly, captured the emergence of extended “peninsula-like” structures within the A compartment during early S phase. In G2, the models showed a more uniform folding pattern accompanied by overall chromosomal compaction (**Fig. 6A**).

To quantitatively assess the formation of "peninsula-like" structures, we measured global A-domain extension, defined as the size-normalized shortest boundary-to-center distance. Analysis of small (1–5 Mb) and large (> 5 Mb) domains revealed that only large A domains showed a significant increase in global extension from late G1 to early S-phase (**Fig. 6B, left panels**). Importantly, this extension occurred without changes in the inter-boundary distance (**Fig. 6B, right panels**), supporting a model in which internal chromatin regions extend outward from anchored boundaries from late G1 to early S—a global spatial reorganization specific to domains larger than 5 Mb.

We next asked whether B compartment domains underwent similar global structural changes. In stark contrast to A domains, they exhibited a significant decrease in both center-to-boundary and boundary-to-boundary distances across all domain sizes (1–5 Mb and > 5 Mb), reflecting global chromatin compaction during the late G1 to early S transition (**Fig. 6C**).

Having established that both A and B domains undergo major global reorganization from late G1 to early S, we next examined whether these structural changes in A and B domains were accompanied by alterations in local chromatin compaction (i.e., changes in the physical packing of the polymer-like fiber). To assess this, we calculated the average bin-to-bin distance within size-stratified domains as a proxy for

local compaction levels. A decrease or increase in this metric would reflect tighter or looser local packing, respectively, whereas stable values would indicate unchanged local packing at this scale.

In A-compartment domains, significant changes in local compaction levels were detected only between early and mid-G1 (decompaction) and between late S and G2 (compaction), with compaction levels converging to a uniform state across domains in G2 (as indicated by the minimal dynamic range), reaching values comparable to those of B domains (**Fig. 6D, Fig. S12A,B**). However, A-domain local compaction remained essentially unchanged from late G1 through S phase, despite substantial global structural reorganization of these domains. Thus, the emergence of “peninsula-like” structures in large A domains reflects global positional rearrangements rather than changes in local chromatin compaction.

As expected, B domains were generally more compact than A domains across all cell-cycle stages (**Fig. 6D, Fig. S12A**). However, their most significant local compaction shift occurred specifically between late G1 and early S, becoming more uniformly compact at the onset of S-phase (**Fig. 6D, right panels; Fig. S12C**). This finding implies a previously unrecognized active contribution of B-compartment domain reorganization in S-phase-dependent compartment maturation.

Taken together, these results refine our understanding of A/B compartment structural dynamics throughout interphase. The simulations not only recapitulated known features, such as chromosome decompaction from early to late G1, but also uncovered previously underappreciated aspects of compartment maturation during S-phase. Specifically, they revealed global changes in the spatial trajectory of A-domain chromatin without local chromatin compaction changes, providing a mechanistic explanation for the gain of long-range interactions and the emergence of consolidated A-compartment domains observed in S-phase (described in the previous section). Moreover, our analyses revealed that B-domains are also actively engaged in compartment maturation, showing more uniform compaction locally and globally in early S, an aspect previously overlooked by conventional Hi-C analyses. Finally, our analyses showed that the G2 phase is characterized by uniformly compact local chromatin across the genome.

Discussion

In this study, we established a simple cell sorting and chromatin profiling strategy that precisely resolves cell-cycle phases across the entire interphase. Using this system, we could capture cell populations with exceptionally high temporal resolution, achieving sub-hour resolution within the G1 phase (**Fig. 1, Fig. S2**). By applying comprehensive, A/B compartment-centric analyses to these carefully staged populations, we obtained a nuanced view of how nuclear organization is dynamically remodeled throughout interphase. This approach allowed us to propose a revised model of cell cycle-dependent chromatin dynamics that challenges the prevailing view (**Fig. 7**). Our model delineates a stepwise cell cycle phase-dependent reorganization of nuclear compartmentalization, comprising four distinct stages. The first stage, chromosome unfolding, occurs from early to late G1 phase as chromatin expands from its highly compacted mitotic state. This is followed by compartment maturation, a sudden enhancement of A/B compartment separation at the onset of S-phase. The third stage, compartment stabilization, persists throughout S-phase, and finally, chromosome refolding is seen during G2 as the cell prepares for mitosis. Our primary focus was on the previously overlooked maturation stage, which we characterized in detail. We found that this reorganization is a direct consequence of S-phase entry but occurs independently of ongoing DNA synthesis. A defining feature of this stage is the formation of a consolidated A compartment, involving extensive spatial reorganization of individual A domains and the establishment of extensive long-range A-A interactions.

Our findings provide several key conceptual insights. While the M-to-G1 and G2-to-M phase transitions are well known for their dramatic chromatin reorganization, we contend that the G1-to-S transition is equally critical yet remains significantly underexplored. This period may represent a rich time window for discovering and characterizing novel 3D genome regulators. Importantly, our results identify S-phase entry as a major driving force of large-scale 3D genome reorganization, prompting a reconsideration of how replication and chromatin architecture are functionally linked.

The prevailing view holds that replication timing is a readout of a pre-established nuclear framework defined by stable compartments and domains[14,27–29]. However, our data indicate that this hierarchy warrants re-evaluation. We propose a model of dynamic interplay, in which chromatin modifications associated with G1-to-S transition actively reshape the very architectural landscape from which the replication program itself is derived. Our results also reveal an unexpected plasticity of A/B compartment organization, even within a single cell type, an aspect often overlooked due to the predominant focus on Hi-C PC1 of asynchronously growing cell populations when assessing A/B compartments. This finding underscores that, while the field increasingly pursues ever-higher data resolution at sub-TAD and loop levels, there remains much to learn about chromatin structure at a global scale. High-resolution approaches, though valuable, should not overshadow the importance of coarse-grained perspectives, as demonstrated by our findings. Finally, it is important to note that our analysis, although based on highly resolved and precisely staged cell populations, remains an ensemble measurement. Future studies combining ultra-high temporal resolution with single-cell analysis will be essential to resolve the precise kinetics and cell-to-cell heterogeneity of these cell cycle-dependent chromatin reorganization events.

Biologically, this dynamic S-phase chromatin behavior raises the question of its functional significance, prompting us to speculate on the roles this reorganization may serve. One plausible role is to facilitate DNA replication: A-compartment regions are gene-rich, euchromatic, and replicate early in S-phase. Their active reorganization during early S could enhance the accessibility or spatial coordination of replication origins and associated factors. It is tempting to speculate that this reorganization supports the formation of coupled replication factories, where sister replisomes function as a single coordinated unit[30], which would promote efficient initiation and smooth progression of replication forks. Such structural flexibility may help optimize replication efficiency and ensure faithful execution of the replication timing program.

A second possibility is that this remodeling improves coordination between replication and transcription. Given that A-compartment regions are also transcriptionally active, their reorganization during replication may help alleviate topological conflicts between transcriptional and replication machineries, allowing both processes to proceed efficiently. Moreover, the rearrangement of A domains could expand the effective interface with nuclear bodies such as splicing speckles, thereby promoting compartmental segregation and optimizing functional compartmentalization during the critical process of DNA replication. These interpretations align with recent work demonstrating that the relative positioning of genomic regions with respect to nuclear locales influences genome organization, replication timing regulation, and gene expression[31].

Uncovering the biological significance of these chromatin dynamics first requires identifying the molecular factors responsible for compartment maturation in S-phase. Components of the replication machinery (particularly those not directly involved in DNA synthesis) represent an intriguing class of potential regulators. Their potential to influence higher-order chromatin organization is supported by recent findings, including evidence that certain replisome components in *Drosophila* undergo phase separation and that replisome loading can restrict chromatin motion independently of DNA synthesis[32]. Beyond the core replisome, other S-phase-associated factors and molecular processes—such as transcriptional machinery, chromatin modifiers, architectural proteins, and nuclear organizers—are also plausible candidates[33,34].

Elucidating the precise roles and interplay of these components will be an important next step in understanding the mechanistic basis of compartment maturation.

While our work primarily focused on the critical G1-to-S transition, events occurring during S-to-G2 transition warrant equal attention. We speculate that mitotic chromosome reformation may begin in G2—potentially earlier than currently appreciated—to facilitate more efficient chromosome segregation. Such early initiation would likely minimize disruption to ongoing nuclear processes. Accordingly, the S/G2 boundary represents another promising window for investigating cell-cycle dependent chromatin reorganization. In summary, our findings support a dynamic, cell-cycle-aware model of A/B compartmentalization, in which chromatin architecture is precisely tuned to accommodate and coordinate essential nuclear functions at the appropriate time.

Materials and methods

Derivation and culture of mESC lines

The R26p-Fucci2 mESC line was obtained from the RIKEN BDR animal facility, LARGE (derived from the R26p-Fucci2 mouse line, Acc. No. CDB0203T). To perform accurate flow cytometry (FACS) color compensation for this dual-reporter line, we also derived control mESC lines from single-reporter mice. For this, oocytes from R26-mCherry-hCdt1(30/120) (Fucci-red, Acc. No. CDB0264K) and R26-mVenus-hGeminin(1/110) (Fucci-green, Acc. No. CDB0265K) mice were fertilized and cultured *in vitro* at the LARGE facility to the morula/blastocyst stage. The zona pellucida was removed using Tyrode's solution (Sigma, T1788). Individual blastocysts were plated onto a feeder layer of mitotically inactivated mouse embryonic fibroblasts (MEFs) in ES cell derivation medium. The medium was composed of KnockOut™ DMEM (ThermoFisher, 10829018) supplemented with 20% knockout serum replacement (KSR, Gibco,10828-028), 1x MEM Non-Essential Amino Acids (Nacalai, 06344-56), 1x EmbryoMax® Nucleosides (Millipore, ES-008-D), 0.5 mg/mL penicillin-streptomycin (Nacalai, 09367-34), 100 µM beta-mercaptoethanol (Gibco, 21985-023), 1 µM PD0325901 (Wako, 162-25291), 3 µM CHIR99021 (Wako, 034-23103), and 1000 U/mL leukemia inhibitory factor (LIF, Nacalai, NU0012-2). After 5–7 days of incubation at 37°C with 5% CO□, the inner cell mass outgrowth was dissociated and replated. Emerging mESC colonies were selectively picked, expanded, and passaged to establish stable cell lines. The mouse ESC lines R26-mCherry-hCdt1 (Fucci-red), R26-mVenus-hGeminin (Fucci-green), R26p-Fucci2, and CBMS1[35] (non-fluorescent) were maintained in 2i/LIF medium. This medium consisted of NDiff 227 base medium (Cellartis, Y40002) supplemented with the following: the two inhibitors (2i) PD0325901 at 1 µM and CHIR99021 at 3 µM; 0.5 mg/mL penicillin-streptomycin; 0.1 mM 2-mercaptoethanol; and LIF at 1000 U/mL. Cells were cultured on iMatrix-511 (Matrixome, 892012)-coated dishes at 37°C with 5% CO□ and passaged every 2–3 days using trypsin/EDTA (Nacalai, 32777-44).

Flow cytometry

Cell sorting and analysis were conducted using a Sony MA900 cell sorter. The following laser and filter configurations were used: mVenus (488-nm laser, 525/50 nm filter), mCherry (561-nm laser, 617/30 nm filter), Hoechst 33342 and FxCycle Violet (405-nm laser, 450/50 nm filter), and Alexa Fluor 647 (638-nm laser, 665/30 nm filter). For color compensation, formaldehyde-fixed CBMS1 mESCs served as a double-negative control. Single-color controls were established using formaldehyde-fixed Fucci-red mESCs, Fucci-green mESCs, and, where applicable, EdU(AF 647)-labeled CBMS1 mESCs. Data were analyzed using FlowJo (v10.8.1).

Live-cell imaging of Fucci mESCs

Fucci mESCs were plated at a density of 0.1 million cells/mL in a 12-well plate and allowed to adhere for several hours prior to imaging. Live-cell imaging was performed for 50 hours using the Celldiscoverer 7 automated microscope (Zeiss), acquiring images every 10 minutes. Imaging was conducted with a 20x objective (NA 0.5) using the system's automated focus maintenance. Fluorescence of the Fucci reporters was captured using the following settings: mCherry was excited with a 590 nm LED and emission was collected with a 635/50 nm bandpass filter; mVenus was excited with a 520 nm LED and emission was collected with a 540/25 nm bandpass filter. Simultaneous transmitted light images were acquired using both Differential Interference Contrast (DIC) and Phase Contrast modalities. For the analysis of the live-cell imaging data, manual tracking of nuclei was performed using the TrackMate plugin (v6.0.30) in Fiji using DIC and phase contrast images (tracker radius was set to 5 pixels). Only cells that completed a full cell cycle, defined as starting two frames after cell division and ending at the last frame before the subsequent cell division, were analyzed. The mean fluorescence intensities (mVenus and mCherry) for each tracked nucleus were exported using the TrackMate Extras plugin. Subsequent data processing and analysis were performed in R (v4.3.2). Briefly, the data from two biological replicates were merged, and

cell cycle trajectories were aligned to the start of G1 phase. Fluorescence signals were baseline-corrected by subtracting the minimum intensity for each channel per cell. This pipeline was used to quantify cell cycle length, G1 length (timing of when cells reach maximum mCherry intensity), and to plot the normalized Fucci fluorescence dynamics.

EdU labeling and detection

To correlate Fucci markers with S-phase progression, DNA synthesis was assessed using the Click-iT Plus EdU imaging kit (Invitrogen). For imaging, cells were plated on sterile glass coverslips 24 hours prior to experimentation. Cells were pulsed with 10 µM EdU for 15 minutes, then fixed with 4% formaldehyde and permeabilized with 0.5% Triton X-100. The Click-iT reaction was performed according to the manufacturer's protocol, incubating cells with the Alexa Fluor 647 azide dye for 30 minutes in the dark. Nuclei were counterstained with Hoechst 33342 (1 µg/mL), and coverslips were mounted with Vectashield antifade mounting medium (Vector Laboratories no. H1000). Imaging was performed on a Nikon Ti-E Eclipse microscope equipped with a SOLA SE LED light source and standard filter sets for DAPI, FITC, TRITC, and Cy5. Images were acquired with a 40x objective and analyzed with the Fiji software (ImageJ2, v2.16.0). For parallel analysis by flow cytometry, cells were harvested and processed in suspension, undergoing the same EdU labeling, fixation, permeabilization, and Click-iT reaction steps using the analogous Click-iT Plus EdU flow cytometry kit (Invitrogen), before being stained for DNA content with 1 µM FxCycle Violet stain (ThermoFisher).

Cell cycle synchronization and collection for Hi-C

For Hi-C experiments, Fucci mESCs were collected under three primary conditions. First, to obtain cells at various cell cycle stages (EG1, MG1, LG1, ES, MS, LS, and G2), an asynchronous population was harvested directly (50-100 million cells per experiment). Second, for the G1/S time-course experiment, cells were synchronized at the G2/M border using a 10-hour treatment with 50 ng/mL Nocodazole (Sigma, M1404). One dish of these synchronized cells was harvested as the G2/M time point. In parallel, other synchronized dishes were washed twice with PBS and released into a medium containing 2.5 mM thymidine (Sigma, T1895); these were then harvested every 3 hours from 3 to 12 hours post-release (collecting 2-4 million cells per time point). Finally, for a G1 arrest time-course, asynchronous mESCs from separate dishes were treated with 1 µM INK-128 (MedChemExpress, HY-13328) and harvested at 24, 72, and 120-hour time points (collecting 2–4 million cells per time point). All collected samples from these procedures were processed for Hi-C and subsequent FACS analysis as described in the following section.

Sample preparation for Hi-C

All harvested cells were processed for Hi-C using an established protocol[36] with minor modifications. Briefly, harvested cells were fixed in 1% formaldehyde in PBS for 10 minutes at room temperature, using 1 mL of fixative per 1 million cells. The reaction was quenched with 0.125 M glycine. After permeabilization with 0.1% saponin, cells were stained with Hoechst33342 (10 µg/mL) for 30 minutes in the dark to label DNA for cell cycle analysis. Cells were then FACS-sorted using a Sony MA900 cell sorter in purity mode. Laser configurations were as previously described in the 'Flow Cytometry' section, and the gating strategies for isolating specific cell cycle populations are detailed in the Results section and corresponding figures. Sorted cell pellets were immediately flash-frozen in liquid nitrogen and stored at –80°C until Hi-C and library preparation. Then, Hi-C libraries were prepared from 0.5–1 million fixed cells (frozen pellets) according to an established protocol[36]. In brief, nuclei were isolated, chromatin was digested with DpnII (NEB, R0543), and restriction fragment overhangs were filled with biotinylated nucleotides prior to blunt-end ligation. After reverse crosslinking and DNA purification, 0.5–1 µg of DNA was sheared to 150–400 bp fragments using a Covaris S220 sonicator, with size selection performed

using AMPure XP beads (Beckman Coulter). Biotin-labeled fragments were captured on Streptavidin-coated magnetic beads (Dynabeads M-280), and the resulting libraries were prepared for sequencing using the NGS LTP Library Preparation Kit (KK8232). Final libraries were sequenced on a NovaSeq X platform to generate 150 bp paired-end reads (approximately 100 million reads per sample; range 70–130 million).

Hi-C data processing and quality control

Hi-C sequencing reads were processed using the 'FANC' pipeline[37] (v0.95) (https://github.com/vaquerizaslab/fanc) with the command: 'fanc auto <fastq1> <fastq2><output> -g mm9 -i <bwa_index> -r MboI -n -b 1mb,200kb -t 30 -f --fanc-parallel -tmp -q 30'. This command performs alignment to the mm9 genome using BWA (v0.7.17), enables iterative mapping (--iterative) with a quality cutoff of 30 (-q 30), and produces a valid pairs file (.pairs) of aligned reads alongside unbinned .hic files. These were then used to generate normalized (-n) contact matrices at 1-Mb and 200-kb resolutions (-b 1mb,200kb). When applicable, biological replicates were merged into a single contact map using 'fanc hic <file1> <file2> <output> -b 1mb -a -n --restore-coverage', where the -a flag aggregates contacts and --restore-coverage maintains library size after merging. Library quality was assessed using 'fanc pairs -s' for mapping statistics and 'fanc hic -s' for cis-chromosomal contacts (see **Table S2** for all quality metrics).

single-cell Hi-C data processing

Multiplexed FASTQ files from Nagano *et al*.[12] were downloaded from GEO (GSE94489). This dataset consists of pooled single-cell libraries, where cells were sorted and sequenced collectively by cell cycle phase. Data were processed identically to our in-house data, with the exception that iterative mapping was omitted and the restriction enzyme was specified as MboI. A summary of downloaded datasets and processing statistics is provided in **Table S3**.

HiRES data processing

Public single-cell sequencing data from the Liu et al. HiRES study[23] were obtained from GEO (GSE223917). This dataset contained a mixture of DNA and RNA sequences. Metadata (science.adg3797_table_s2.xlsx) were filtered to select specific cell types and developmental stages (ExE endoderm E75, Mixed late mesenchyme, Neural ectoderm E75, Neural tube E85) with sufficient sequencing depth (> 100 million reads across G1 and mid S cell populations). Individual cell IDs were extracted, and corresponding FASTQ files were downloaded. Adapter trimming was performed with Cutadapt (v1.18) using the RNA-specific sequence (GGTTGAGGTAGTATTGCGCAATG) to discard non-ligated RNA fragments (--discard-trimmed) and isolate DNA-derived Hi-C pairs. Read quality was assessed using FastQC (v0.11.9). Per-cell-type replicates were generated by merging forward (_1_DNA.fastq.gz) and reverse (_2_DNA.fastq.gz) reads from individual cells. The resulting merged FASTQ files were once again assessed using FastQC and then processed through the FANC pipeline using the MboI restriction enzyme site, without iterative mapping (see **Table S1** for sample details and statistics).

Probability (P(s)) plots derivation

Contact probability (P(s)) curves were generated using FANC's expected value calculation (fanc expected). The analysis was performed on 1-Mb resolution Hi-C matrices, comparing the decay of contact probability as a function of genomic distance (s) for each tested condition. The resulting P(s) curves were plotted to visualize differences in interaction frequency decay across conditions.

Contact map comparisons

Pairwise comparisons between Hi-C matrices were performed using the 'fanc compare' function. Matrices at 200-kb resolution were directly compared using the -Z (z-score normalization) and -I (insulation correction) parameters. The resulting difference matrices were visualized using the 'fancplot' function to highlight regions of increased or decreased contact frequency between two conditions.

Principal component analysis (PCA) of Hi-C matrices

Principal component analysis was performed on 1-Mb resolution Hi-C contact matrices from all biological replicates using FANC's PCA implementation (fanc pca)[37], analyzing the top 50,000 genomic bins (default parameter). The analysis included all chromosomes with a minimum distance cutoff of 1 Mb.

A/B Compartment analysis and saddle plot generation by FANC

A/B compartments were called from Hi-C contact matrices at 1-Mb resolution using the 'fanc compartments' command. A Pearson correlation matrix was calculated from the .hic file. The first eigenvector (PC1) was computed from this matrix and its sign was oriented using the GC content of the mm9 genome (-g option). The oriented PC1 and the resulting A/B compartment domain coordinates were output to BED files (-v and -d options, respectively).

Saddle plots were generated from the compartment eigenvector (1-Mb resolution) using the 'fanc compartments' command. The -e option was used to output the enrichment plot, and the --compartment-strength option was used to calculate a quantitative compartment strength score (as defined by Flyamer et al.[38] as the natural logarithm of $AA * BB / AB^2$). Compartments were binned into 5-percentile intervals using the -p option, and the resulting enrichment matrix was saved to a file with the -m option for downstream analysis.

t-SNE and K-means clustering of saddle plots

Saddle plot enrichment matrices at 1-Mb resolution were analyzed in R using t-distributed stochastic neighbor embedding (t-SNE) and K-means clustering. Individual matrices were flattened into vectors and dimensionality reduction was performed with perplexity 7 and 500 iterations. K-means clustering (k=2) was then applied to the resulting coordinates to identify groups of samples with similar compartment interaction patterns.

Format conversion for subsequent Hi-C analysis

Hi-C pairs were converted from FANC's proprietary format to the standardized .pairs format and processed as individual replicates into multi-resolution cooler matrices (.mcool) using cooler[39] (v0.9.3) 'cload pairs' and 'zoomify'. When applicable, biological replicates were merged at 10-kb resolution using 'cooler merge', and the resulting combined matrix was processed with 'cooler zoomify' using identical parameters (resolutions from 10 kb to 1 Mb with iterative balancing) to generate the final merged .mcool file.

Calculation of contact probability decay profiles

Contact decay profiles were generated from the same standardized .pairs files. A 10% downsampling of each file was performed using 'pairtools sample' (v0.3.0) with a random seed of 1 to ensure reproducibility and facilitate computational efficiency. The resulting downsampled pairs files were processed with a custom R script to calculate the contact probability as a function of genomic distance, adapted from the method described by Nagano *et al.*[12]. For each read pair, the linear genomic separation was calculated for intra-chromosomal (cis) interactions. These distances were log2-transformed and binned. The contact frequency for each bin was normalized by the total number of valid cis reads to generate a relative contact probability. Finally, the decay profiles were visualized as a heatmap using the 'fields' package in R,

where the x-axis represents different cell cycle phases, the y-axis represents genomic distance, and the color intensity corresponds to the percentage of total contacts.

Compartment calling at 200-kb resolution

Although compartment calling is available in the standard 'FANC' pipeline, we found that compartments were not robustly called at 200-kb resolution. To address this, we performed compartment analysis using a custom Python implementation that executes principal component analysis (PCA) via cooltools (0.3.2). Compartments were called from balanced .mcool files using a modified approach that calculates principal components through correlation and covariance matrices before PCA. The first principal component (PC1) was extracted as the compartment track, where positive values correspond to active (A) compartments and negative values to inactive (B) compartments. PC1 sign was oriented using a gene density track for mm9. The analysis calculated three key outputs for each sample: compartment eigenvectors, eigenvalues, and the eigenvalue contribution rate for PC1, which quantifies the proportion of variance in the contact matrix explained by A/B compartmentalization (PC1).

Hierarchical clustering of compartment profiles

A/B compartment profiles at 200-kb resolution were analyzed using DeepTools (v3.5.5). First, compartment eigenvectors were summarized using 'multiBigwigSummary bins' across all samples. Pearson correlation coefficients were then calculated and visualized as a clustered heatmap using 'plotCorrelation' with outlier removal.

Quantification of compartment smoothness using mean-square-gradient (MSG)

To quantitatively assess the smoothness of A/B compartment profiles, we calculated the mean-square-gradient (MSG) of the compartment signal (PC1) derived from 200-kb binned data. The MSG is defined as MSG = □$(\partial f/\partial x)^2$□, where f(x) is the compartment signal as a function of genomic position x. This metric quantifies the average rate of change of the compartment signal, where higher values indicate more variable, less smooth signals, while lower values reflect more uniform, smoother compartment signals. The genomic gradient of PC1 was computed for all chromosomes in each cell cycle stage using the 'numpy.gradient' function in Python. To focus on core compartment domains while avoiding boundary regions, we selected genomic bins where the compartment signal exceeded one standard deviation above the chromosome mean for A compartments, or fell below one standard deviation for B compartments. The MSG was calculated separately for these strong A (MSG_A,1σ) and B (MSG_B,1σ) regions. To measure the relative changes in compartment signal smoothness throughout the cell cycle and normalize for technical variations, we computed the ratio MSG_A,1σ/MSG_B,1σ.

Distance-based compartment strength quantification

We used 'Pentad'[25] (github.com/magnitov/pentads, commit 66c19f4) to measure A/B compartment interactions at various genomic distances. Hi-C contact matrices in .mcool format and compartment signals (PC1) at 200 kb resolution were used as input for Pentad's cis-interaction scripts (get_pentad_cis.py) with rescaling to 50 matrix (pixel) bins. Compartment strength was quantified (quant_strength_cis.py), and distance-dependent analyses were performed at 1, 10, 25, and 50 Mb distances (get_pentad_distance.py). Subsequent analysis in R compared chromosome-specific strength values for inter- and intra-compartment interactions (A-A, B-B, A-B) across cell cycle phases. Delta median values were calculated for consecutive cell cycle transitions to identify the magnitude of change in compartment strength.

Chromatin subcompartment analysis

Chromatin subcompartments were identified using 'CALDER2'[20] (https://github.com/CSOgroup/CALDER2) executed within a Docker container (lucananni93/calder2:latest). For compatibility with CALDER, contact matrices in .mcool format were converted to .hic files using 'cooler dump' to export balanced interaction scores, followed by conversion with juicer_tools (v1.22.01) using the mm9 genome assembly. Analyses were performed at 40-kb resolution for newly generated data and 200 kb for reanalyzed HiRES data, with binning chosen to ensure a strong correlation of compartment rank with a reference dataset (Pearson's rho > 0.4). Subcompartment calls were filtered in R to include only genomic bins consistently detected across all cell cycle fractions. Subcompartment sizes were calculated as contiguous genomic regions sharing identical compartment ranks within the hierarchical system spanning eight ranks (0.125–1), representing the continuum from B-compartments (0.125–0.5) to A-compartments (0.625–1).

3D Genome structure modeling from Hi-C data

Chromosome structures were reconstructed from Hi-C data using 'GenomeFlow' (v2.0) (https://github.com/jianlin-cheng/GenomeFlow) with the 'LorDG-3D Modeler' function[26]. We generated intra-chromosomal contact maps from 200-kb resolution Hi-C matrices using 'fanc dump --only-intra' and separated them into individual chromosome datasets. For each chromosome, 10,000 iterations of the modeling algorithm were performed with an optimized conversion factor of 0.6 to maximize the correlation between reconstructed 3D distances and original Hi-C interaction frequencies. A/B compartment annotations were derived from Calder subcompartment calls (200-kb resolution) and stitched into continuous A or B domains using custom R scripts. Spatial coordinates (x, y, z) were extracted for each 200-kb genomic bin, annotated with A/B compartment identity, and filtered to retain only bins common to all samples. From these structural models, we quantified 3D compartment organization for domains > 1 Mb using three spatial metrics calculated from the relative 3D Euclidean distances (in arbitrary units, a.u.) in the reconstructed models:

1. Local compaction: The mean 3D Euclidean distance between all consecutive bins within a domain.
2. Domain shape: The average 3D distance from the domain boundaries to its central bin.
3. Inter-boundary distance: The 3D distance between the leftmost and rightmost boundary bins.

Boundary-to-center and inter-boundary distances were normalized by the number of bins per domain. Statistical significance was assessed using Wilcoxon rank-sum tests with Benjamini-Hochberg correction.

Statistics and reproducibility

All statistical analyses are detailed in the figure legends and main text. This includes the specific tests used, the number of independent biological replicates (N), the number of technical measurements or data points (n), and either exact P-values (P) or standard significance indicators (ns, not significant; $P \leq 0.05$; $^{*}P \leq 0.01$; $^{**}P \leq 0.001$; $^{***}P \leq 0.0001$). In box plots, the central line denotes the median, the box boundaries represent the 25th and 75th percentiles, and the whiskers extend to the most extreme data points within 1.5 times the interquartile range from the box.

Acknowledgements

We are grateful to all members of the Hiratani laboratory for their insightful discussions and feedback throughout this project. We extend special thanks to Y. Furuta, H. Kiyonari, and M. Kaneko (RIKEN BDR animal facility, LARGE) for providing the Fucci2 mESCs and T. Abe for single Fucci reporter blastocysts. We also thank S. Takahashi and A. Ueno for their technical assistance in deriving mESCs from blastocysts; R. Poonperm for experimental and analytical support; and M. Takiguchi for technical assistance with live-cell imaging on the CellDiscoverer7 microscope. Finally, we thank T. Takahashi, Y.

Kawasoe, A. Sakaue-Sawano, A. Miyawaki, Y. Wang, J. Cheng, and M. Magnitov for their valuable scientific input. We also acknowledge the use of large language models, specifically ChatGPT (OpenAI), Gemini (Google), DeepSeek (DeepSeek-AI), and Perplexity AI, to assist with the editing of the manuscript text, as well as for troubleshooting code during data analysis. The authors reviewed, edited, and take full responsibility for all content. This work was supported by a RIKEN International Program Associate (IPA) fellowship to L.C.; RIKEN BDR intramural grants, the RIKEN Pioneering Project 'Genome Building from TADs', MEXT KAKENHI Grant Number JP18H05530, JSPS KAKENHI Grant Numbers JP20K20582 and JP25H00982, and JST CREST Grant Number JPMJCR20S5 to I.H.

Author contributions

L.C. and I.H. conceived the study. L.C. designed and performed the majority of the experimental work and conducted the bioinformatic analyses. Hi-C experiments were performed jointly by L.C. and T.I. H.M. generated key preliminary data and facilitated data conversion between analytical platforms. A.O. characterized the INK-128-induced G1-like arrest in detail and provided experimental support and R.C. performed MSG analysis and generated the panels in Fig. S9. The manuscript was written by L.C. and I.H. with input from all co-authors.

Competing interests

The authors declare no competing interests.

Data availability

The raw Hi-C sequencing data have been deposited in the DNA Data Bank of Japan (DDBJ) under BioProject accession PRJDB37948. The processed Hi-C data are available in the Gene Expression Omnibus under accession GSE312348. The live-cell imaging and single-cell tracking data (Fucci-mESCs) are available at Zenodo: https://doi.org/10.5281/zenodo.17509931.

References

1. Cremer, T. & Cremer, C. Chromosome territories, nuclear architecture and gene regulation in mammalian cells. *Nat Rev Genet* **2**, 292–301 (2001).
2. Bonev, B. & Cavalli, G. Organization and function of the 3D genome. *Nat Rev Genet* **17**, 661–678 (2016).
3. Lieberman-Aiden, E. *et al.* Comprehensive Mapping of Long-Range Interactions Reveals Folding Principles of the Human Genome. *Science* **326**, 289–293 (2009).
4. van Steensel, B. & Belmont, A. S. Lamina-Associated Domains: Links with Chromosome Architecture, Heterochromatin, and Gene Repression. *Cell* **169**, 780–791 (2017).
5. Naumova, N. *et al.* Organization of the Mitotic Chromosome. *Science* **342**, 948–953 (2013).
6. Gibcus, J. H. *et al.* A pathway for mitotic chromosome formation. *Science* **359**, eaao6135 (2018).
7. Samejima, K. *et al.* Rules of engagement for condensins and cohesins guide mitotic chromosome formation. *Science* **388**, eadq1709 (2025).
8. Abramo, K. *et al.* A chromosome folding intermediate at the condensin-to-cohesin transition during telophase. *Nat Cell Biol* **21**, 1393–1402 (2019).
9. Zhang, H. *et al.* Chromatin Structure Dynamics During the Mitosis to G1-Phase Transition. *Nature* **576**, 158–162 (2019).
10. Kang, H. *et al.* Dynamic regulation of histone modifications and long-range chromosomal interactions during postmitotic transcriptional reactivation. *Genes Dev* **34**, 913–930 (2020).
11. Pelham-Webb, B. *et al.* H3K27ac bookmarking promotes rapid post-mitotic activation of the pluripotent stem cell program without impacting 3D chromatin reorganization. *Mol Cell* **81**, 1732-1748.e8 (2021).
12. Nagano, T. *et al.* Cell-cycle dynamics of chromosomal organisation at single-cell resolution. *Nature* **547**, 61–67 (2017).
13. Hiratani, I. *et al.* Global Reorganization of Replication Domains During Embryonic Stem Cell Differentiation. *PLOS Biology* **6**, e245 (2008).
14. Pope, B. D. *et al.* Topologically associating domains are stable units of replication-timing regulation. *Nature* **515**, 402–405 (2014).
15. Cooper, S. Rethinking synchronization of mammalian cells for cell cycle analysis. *Cell Mol Life Sci* **60**, 1099–1106 (2003).
16. Sakaue-Sawano, A. *et al.* Visualizing Spatiotemporal Dynamics of Multicellular Cell-Cycle Progression. *Cell* **132**, 487–498 (2008).
17. Abe, T. *et al.* Visualization of cell cycle in mouse embryos with Fucci2 reporter directed by Rosa26 promoter. *Development* **140**, 237–246 (2013).
18. Boward, B., Wu, T. & Dalton, S. Concise Review: Control of Cell Fate Through Cell Cycle and Pluripotency Networks. *Stem Cells* **34**, 1427–1436 (2016).
19. Manders, E. M. M., Kimura, H. & Cook, P. R. Direct Imaging of DNA in Living Cells Reveals the Dynamics of Chromosome Formation. *J Cell Biol* **144**, 813–822 (1999).
20. Liu, Y. *et al.* Systematic inference and comparison of multi-scale chromatin sub-compartments connects spatial organization to cell phenotypes. *Nat Commun* **12**, 2439 (2021).
21. Meshorer, E. *et al.* Hyperdynamic Plasticity of Chromatin Proteins in Pluripotent Embryonic Stem Cells. *Developmental Cell* **10**, 105–116 (2006).
22. Bonev, B. *et al.* Multiscale 3D Genome Rewiring during Mouse Neural Development. *Cell* **171**, 557-572.e24 (2017).
23. Liu, Z. *et al.* Linking genome structures to functions by simultaneous single-cell Hi-C and RNA-seq. *Science* **380**, 1070–1076 (2023).
24. Boroviak, T., Loos, R., Bertone, P., Smith, A. & Nichols, J. The ability of inner-cell-mass cells to self-renew as embryonic stem cells is acquired following epiblast specification. *Nat Cell Biol* **16**, 516–528 (2014).
25. Magnitov, M. D., Garaev, A. K., Tyakht, A. V., Ulianov, S. V. & Razin, S. V. Pentad: a tool for distance-dependent analysis of Hi-C interactions within and between chromatin compartments. *BMC Bioinformatics* **23**, 116 (2022).
26. Trieu, T., Oluwadare, O., Wopata, J. & Cheng, J. GenomeFlow: a comprehensive graphical tool for modeling and analyzing 3D genome structure. *Bioinformatics* **35**, 1416–1418 (2019).

27. Dimitrova, D. S. & Gilbert, D. M. The spatial position and replication timing of chromosomal domains are both established in early G1 phase. *Mol Cell* **4**, 983–993 (1999).
28. Dileep, V. *et al.* Topologically associating domains and their long-range contacts are established during early G1 coincident with the establishment of the replication-timing program. *Genome Res* **25**, 1104–1113 (2015).
29. Miura, H. *et al.* Single-cell DNA replication profiling identifies spatiotemporal developmental dynamics of chromosome organization. *Nat Genet* **51**, 1356–1368 (2019).
30. Liu, Y. *et al.* Fork coupling directs DNA replication elongation and termination. *Science* **383**, 1215–1222 (2024).
31. Gholamalamdari, O. *et al.* Major nuclear locales define nuclear genome organization and function beyond A and B compartments. *eLife* **13**, RP99116 (2025).
32. Pabba, M. K. *et al.* Replisome loading reduces chromatin motion independent of DNA synthesis. *eLife* **12**, RP87572 (2023).
33. van Schaik, T., Vos, M., Peric-Hupkes, D., HN Celie, P. & van Steensel, B. Cell cycle dynamics of lamina-associated DNA. *EMBO reports* **21**, e50636 (2020).
34. Zhang, H. *et al.* CTCF and transcription influence chromatin structure re-configuration after mitosis. *Nat Commun* **12**, 5157 (2021).
35. Murakami, K., Araki, K., Ohtsuka, S., Wakayama, T. & Niwa, H. Choice of random rather than imprinted X inactivation in female embryonic stem cell-derived extra-embryonic cells. *Development* **138**, 197–202 (2011).
36. Kadota, M. *et al.* Multifaceted Hi-C benchmarking: what makes a difference in chromosome-scale genome scaffolding? *Gigascience* **9**, giz158 (2020).
37. Kruse, K., Hug, C. B. & Vaquerizas, J. M. FAN-C: a feature-rich framework for the analysis and visualisation of chromosome conformation capture data. *Genome Biol* **21**, 303 (2020).
38. Flyamer, I. M. *et al.* Single-nucleus Hi-C reveals unique chromatin reorganization at oocyte-to-zygote transition. *Nature* **544**, 110–114 (2017).
39. Abdennur, N. & Mirny, L. A. Cooler: scalable storage for Hi-C data and other genomically labeled arrays. *Bioinformatics* **36**, 311–316 (2020).

Main figure legends

Figure 1. Cell cycle-phased Hi-C reveals a stepwise progression of nuclear compartmentalization
(A-D) Experimental workflow for cell-cycle phase sorting and Hi-C. **(A)** The Fucci2 reporter **(top)** labels cell cycle phases: G1/early S (mCherry-hCdt1, red) and S/G2/M (mVenus-hGeminin, green). Asynchronous mESC cultures expressing this reporter **(bottom)** were fixed, permeabilized, and DNA-stained for FACS sorting.
(B) FACS-sorting strategy for the S and G2 phase cell populations based on DNA content.
(C) Sequential gating strategy to isolate G1 subpopulations: selection of Geminin-negative cells (Gate A), followed by gating on 2C DNA content (Gate B, whole G1 population), and final fractionation into early, mid, and late G1 according to increasing levels of Cdt1-mCherry fluorescence intensity (~30% of the total population per fraction). **(D)** Sorted cells from each defined phase were subject to in-situ Hi-C. **(E)** Contact decay profiles for all cell cycle phases, illustrating a continuum of cis-interactions and a progressive shift from long-range (> 12 Mb) to short-range (< 1 Mb) interactions during the -G1-to-S phase transition.
(F) Contact probability, P(s), plotted against genomic distance on a log-log scale (1-Mb resolution). **(G)** Hi-C contact maps (1-Mb resolution) of chromosome 11 for each cell cycle phase, with the corresponding A/B compartment profiles (Hi-C PC1) shown below each map. The arrows on the Hi-C maps highlight the progressive outward expansion of contact signal from the diagonal, indicating the strengthening of long-range interactions. **(H)** Hi-C saddle plots showing contact enrichment between 1-Mb genomic bins, where both axes are sorted by their Hi-C PC1 value (strongest A to strongest B compartment). The schematic below defines the axis ordering. The overall compartment strength (numerical values in black) and the specific AA, BB, and AB interaction strengths (numerical values in white) are quantified. The color scale represents observed/expected (O/E) contact frequencies in 5-percentile increments. **(I)** Hi-C-based compartment strength dynamics across the cell cycle. Each line represents an independent biological replicate. Data shown in panels **(E–H)** are from biological replicate 1 (representative of N=2 biological replicates). EG1, early G1; MG1, mid G1; LG1, late G1; ES, early S; MS, mid S; LS, late S.

Figure 2. A/B compartment analysis following cell cycle perturbation
(A) Experimental design for time-course Hi-C following treatment with INK-128 (INK). **(B)** Hi-C contact maps (1-Mb resolution) of INK-128-treated cells (24, 72, and 120 h), with corresponding A/B compartment profiles (Hi-C PC1) shown below each map. **(C)** Hi-C saddle plot analysis of compartment strength for the data in (B), quantifying the overall strength (numerical values in black) and specific AA, BB, and AB interaction frequencies (numerical values in white). The color scale represents O/E contact frequencies in 5-percentile increments. **(D)** Experimental design for time-course Hi-C following mitotic arrest with Nocodazole (Noc) and release into a Thymidine (Thy) block. **(E)** Hi-C contact maps and A/B compartment profiles for the experiment in (D). Cell-cycle stages (labeled in pink) were inferred for each population based on Fucci2 reporter fluorescence from FACS analysis. **(F)** Hi-C saddle-plot analysis of compartment strength for the data in (E). **(G)** Principal component analysis (PCA) of Hi-C matrices (1-Mb resolution) from asynchronous cell-cycle phases, Nocodazole-Thymidine-blocked cells, and INK-128-treated time-course samples. PCA sample size=50,000.
Data shown in panels **(B)**, **(C)**, **(E)** and **(F)** are from biological replicate 1 (representative of N=2 biological replicates).

Figure 3. S-phase A-compartment consolidation revealed by subcompartment analysis
(A) IGV browser tracks of Calder subcompartments (40-kb resolution) for the entire chromosome 11 across all cell-cycle stages. **(B)** Abundance of each Calder subcompartment rank, quantified as the total number of 40-kb genomic bins per cell-cycle stage. **(C)** Violin plots with overlaid box plots showing the

size distribution of Calder subcompartment domains in late G1 versus mid-S phase. Domains are defined as contiguous stretches of genomic bins having the same subcompartment rank. Statistical significance was determined using the Wilcoxon rank-sum test; ns, not significant; *$P \leq 0.05$; **$P \leq 0.01$; ***$P \leq 0.001$; ****$P \leq 0.0001$. Data in all panels are from merged biological replicates (N=2).

Figure 4. Pseudo-bulk Hi-C of single cells reveals conserved A-compartment consolidation during S phase across embryonic development

(A) Selection of single-cell populations from Liu et al.[23] (HiRES) data for pseudo-bulk Hi-C analysis. The schematic shows the number of cells and developmental stage for each G1 and mid-S population. E7.5, embryonic day 7.5; ExE, extra-embryonic. **(B)** Hi-C saddle-plot analysis of compartment strength for data generated from the merged single-cell populations in (A) (1-Mb resolution), quantifying overall strength (numerical values in black) and specific AA, BB, and AB interaction frequencies (numerical values in white). The color scale represents O/E contact frequencies in 5-percentile increments. MS, mid S. **(C)** Abundance of Calder subcompartment ranks (200-kb resolution), shown as the total number of genomic bins, comparing G1 and mid-S phases across all four developmental stages.

Figure 5. S-phase A-compartment consolidation involves enhanced long-range contacts and structural reorganization

(A) Cis-by-distance Pentad plots[25] for all cell-cycle stages from early G1 (EG1) to G2 phase for short (1–10 Mb), short-mid (10–25 Mb), mid/long (25–50 Mb), and long-range (> 50 Mb) interactions. The value at the center of each plot indicates the mean O/E contact frequency. **(B)** Hi-C compartment strength for different interaction types (inter-A, intra-A, inter-B, intra-B) across interphase, from early G1 (EG1) to G2 phase. Distributions are shown as violin plots with medians indicated by red bars (each dot represents a single chromosome). Statistical significance between consecutive cell-cycle stages was assessed using pairwise Wilcoxon rank-sum tests. **(C)** Quantification of the Δ median interaction strength between consecutive cell-cycle stages for all interaction types. Inter-A compartment interactions show the largest increase during the late G1-to-early S-phase transition. **(D)** Observed/Expected Hi-C matrices of two representative regions (chr2: 20–40 Mb and chr8:117–131 Mb) in late G1 (LG1) and early S phase (ES), with corresponding PC1 compartment profiles. The right panel shows a differential heatmap (ES – EG1, early S – late G1). Purple circles highlight weakened interactions between boundaries and the center of a large A domain, or intra-A interactions; black rectangles highlight decreased interactions between neighboring A domains, or inter-A interactions. **(E)** Schematic model proposing the "A peninsula" formation, where internal regions of large A compartments extend away from their boundaries during S-phase. Panels **(A–D)** present data from merged biological replicates (N=2) analyzed at 200-kb resolution.

Figure 6. 3D genome modeling from Hi-C recapitulates temporal interphase compartment dynamics

(A) 3D genome structures of chromosomes 2 and 17 across the cell cycle, simulated from Hi-C data using the LorDG Modeler in GenomeFlow[26] using a conversion factor of 0.6 (10,000 iterations). **(B,C) (Left panels)** Quantification of outward extension for compartments A and B, showing the mean shortest Euclidean distance from the domain center to its boundaries (calculated as (d1 + d2)/2), normalized by the number of bins per domain. **(Right panels)** Quantification of boundary movement, showing the shortest Euclidean distance between the boundaries of adjacent domains, normalized by the number of bins per domain. Analyses are shown for small (1–5 Mb) and large (> 5 Mb) domains, comparing late G1 and early S phases. **(D)** Distribution of the mean bin-to-bin distance within A **(Left panels)** and B **(Right panels)** compartment domains across cell-cycle phases. Data are shown for small (1–5 Mb) and large (> 5 Mb) domains. Boxplots in **(B–D)** show the median and quartiles. Each point in the scatter represents a single domain (n = total domains). Pairwise comparisons between consecutive phases were calculated

using the Wilcoxon rank-sum test, and p-values were adjusted using the Benjamini-Hochberg method. Data are from merged biological replicates (N=2), analyzed at 200-kb resolution.

Figure 7. Model of stepwise 3D genome reorganization during the cell cycle

The model proposes four sequential stages: (1) Chromosome unfolding (G1): Gradual formation of long-range interactions from the compact mitotic state. (2) Compartment maturation (G1/S Transition): An abrupt enhancement of compartmentalization upon S-phase entry, independent of DNA synthesis. This stage is characterized by A-compartment consolidation, accompanied by increased long-range A-A interactions and uniform compaction of the B compartment. (3) Compartment stabilization (S-phase): The matured compartment state is maintained throughout the S phase. (4) Chromosome refolding (G2): Global compaction begins in preparation for mitosis.

Supplementary materials:
Supplementary note
Figures S1 to S12
Tables S1 to S3

Supplementary note: A comparison of methodologies for A/B compartment analysis
Our study characterizes compartment dynamics using *de novo* identification of A/B compartments from population Hi-C data. This approach differs fundamentally from the single-cell compartment "strength" metric pioneered by Nagano *et al.* (2017)[12], and the choice of methodology is directly linked to the specific biological question being addressed.
The method developed by Nagano *et al.* was designed to quantify cell-to-cell variation by first defining a stable reference map of A and B domains derived from pooled single-cell data. The compartment strength for each individual cell is then calculated based on how closely its intra-chromosomal contact pattern conforms to this pre-defined reference. This provides a robust measure of structural heterogeneity but inherently assesses fidelity to the population-average architecture, rather than the strength of compartmentalization per se.
In contrast, our *de novo* approach re-identifies compartment identities independently for each cell-cycle-staged population, allowing us to capture the temporal progression of compartment organization, including large-scale rearrangements and the emergence of new organizational states that would otherwise be masked by comparison to a static reference. Thus, while the method of Nagano *et al.*[12] provides an excellent measure of compartment pattern conservation across cells, our approach is specifically tailored to reveal how these patterns evolve over time during cell-cycle progression.

Supplementary figure legends

Figure S1. Fucci marker validation by imaging and FACS
(A) Schematic of the EdU labeling protocol in Fucci mESCs for subsequent FACS or imaging analysis. Steps common to both procedures are shown in black. **(B)** Representative images of Fucci-expressing nuclei (indicated by white arrows) after EdU treatment and DNA labeling across G1, S, G2, and M phases. Scale bar = 10 µm. **(C)** FACS analysis of EdU-labeled Fucci mESCs, showing DNA content **(left)**, EdU versus DNA content with gated cell-cycle populations **(middle)**, and the same EdU versus DNA content plot with overlaid Fucci signals **(right)**. Geminin-mVenus (green) accumulates at the G1/S transition, while Cdt1-mCherry (red) is enriched in G1.

Figure S2. Cell-cycle dynamics of Fucci mESCs measured by time-lapse imaging
(A) Schematic of the time-lapse imaging and cell-tracking strategy. **(B**) Temporal dynamics of Fucci reporters (Geminin-mVenus, green; mCdt1-mCherry, red) in single cells after baseline correction and alignment to cell-cycle start (two frames post cell division). Mitotic cells are excluded. **(C)** Quantification of total cell-cycle length. The mean duration was estimated to be 10.83 ± 2.49 h. **(D)** Distribution of time spent in G1 (red) versus S/G2/M (green). G1 length was defined as the interval from mitosis to the peak of mCherry fluorescence, with the remaining cell cycle duration assigned to S/G2/M phases. Data in **(B–D)** are from tracked cells across 2 biological replicates (n=131).

Figure S3. Hi-C sample QC and supplementary compartment analysis

(A) Principal component analysis (PCA) of replicate Hi-C matrices. The plot shows PCA performed on Hi-C contact matrices (1-Mb resolution) from biological replicates of asynchronous cell-cycle samples, demonstrating replicate concordance. PCA sample size = 50,000. **(B)** Pearson correlation matrix and hierarchical clustering of Hi-C PC1 compartment profiles (1-Mb resolution) for biological replicates R1 and R2. **(C)** Representative IGV browser tracks of Hi-C PC1 compartment profiles (200-kb resolution) for chromosomes 2, 7, and 18. **(D)** Quantification of Hi-C PC1 contribution rates for individual chromosomes throughout interphase for replicate 1 **(top)** and replicate 2 **(bottom)** at 200-kb resolution.

Figure S4. Cell-cycle-phased Hi-C data of individual chromosomes

(A) Hi-C contact maps (1-Mb resolution) of representative chromosomes (chr3, 4, 8, 12, and 19) across cell-cycle phases. **(B)** Contact probability, P(s), versus genomic distance on a log-log scale (1-Mb resolution) for individual chromosomes. Data are from merged biological replicates (N=2).

Figure S5. Re-analysis of single-cell Hi-C data from Nagano *et al.*[12] (pseudo-bulk analysis)

(A) Contact probability versus genomic distance. Log-log plots of P(s) for merged single-cell Hi-C data (1-Mb resolution, N=2 biological replicates). Consistent with our findings, G1 phase exhibits the longest interaction range compared to mid- and late S/G2 phases. **(B)** Principal component analysis (PCA) of Hi-C contact matrices (1-Mb resolution; sample size = 50,000) demonstrates high reproducibility between biological replicates. **(C)** Hi-C contact maps (1-Mb resolution) of representative chromosomes (chr 8, 11, and 15) across cell-cycle phases of replicate 1. **(D)** Compartment strength quantification. Hi-C saddle plots for replicate 1 **(top)** and replicate 2 **(bottom)** at 1-Mb resolution show overall compartment strength (numeric values in black) and specific A-A, B-B, and A-B interaction frequencies (numeric values in white). The color scale represents observed/expected (O/E) contact frequencies in 5-percentile bins. As in our data, A/B compartment strength peaks during S-phase and diminishes in late S/G2.

Figure S6. Reversible G1/G0 arrest of mESCs by INK-128

(A) Schematic of the time-course cell-cycle arrest experiment with INK-128 (1 μM). INK, INK-128. **(B)** Representative images of cells under each condition (numbered as in (A)), with corresponding cell-count quantification (mean ± SD, N=3). **(C)** Cell proliferation following long-term (120 h) INK-128 treatment and release into fresh medium (mean ± SD, N=3). SD, standard deviation.

Figure S7. FACS and Hi-C data analysis after cell-cycle perturbation

(A) FACS analysis of INK-128-treated (G1/G0-arrested) cells. DNA content **(top panel)**, Geminin-mVenus (log scale) versus DNA content **(middle panel)**, and Cdt1-mCherry (log scale) versus DNA content **(bottom panel)**. Purple gates indicate cell populations sorted for Hi-C. **(B)** Contact probability, P(s), versus genomic distance for INK-128-arrested cells (log-log scale, 1-Mb resolution). Data are from single biological replicates of independent experiments (N=2). **(C)** FACS analysis of Nocodazole/Thymidine-treated (G1/S-arrested) cells. Panels are as in (A). Cell-cycle stages (labeled in pink) were inferred for each population based on Geminin and Cdt1 fluorescence. **(D)** Contact probability, P(s), versus genomic distance for G1/S-arrested cells (log-log scale, 1-Mb resolution). Data are from single biological replicates of independent experiments (N=2). **(E)** t-SNE analysis with k-means clustering (k=2) of compartment saddle plot data (1-Mb resolution) from asynchronous cell-cycle samples (early G1, late G1, early S, mid S) and synchronized samples (INK-128-treated and Nocodazole + Thymidine-treated). Labels “1” and “2” denote biological replicates 1 and 2, respectively.

Figure S8. Calder subcompartment organization of representative chromosomes across interphase

IGV browser tracks of Calder subcompartments (40-kb resolution) for representative chromosomes (chr 2, 6, 13 and 15) across all cell-cycle stages. Data are from merged biological replicates (N=2).

Figure S9. Quantification of A/B compartment PC1 signal "smoothness" by mean-square gradient (MSG)

(A) Example genomic region showing Hi-C PC1 compartment profiles on IGV, illustrating smoothness of the A-compartment signal in S phase compared with G1. **(B) (Top)** Two schematic examples of compartment-like signals. The signal on the right is an artificially smoothed version of the signal on the left using a sliding-window average. **(Middle)** The gradient of each curve is plotted, revealing reduced variation in the smoothed curve, while keeping the same vertical limits. **(Bottom)** The squared gradient for each curve is plotted. The corresponding mean-square gradient (MSG) values are indicated. The smooth curve shows an MSG over tenfold lower, demonstrating the utility of MSG for quantifying smoothness. **(C**) Ratio of MSG between strong A (top > 1 SD; SD, standard deviation) and strong B (bottom > 1 SD) compartment signals (Hi-C PC1) for each cell-cycle stage. **(D)** MSG values for compartments defined by different thresholds. From left to right, compartments are defined with increasingly stringent thresholds: the top versus bottom 10%, 5%, 3%, and 2% of Hi-C PC1 values. Data points represent average MSG values. Data in **(C, D)** are from merged biological replicates (N=2), analyzed at 200-kb resolution.

Figure S10. Representative genomic regions showing A-domain reorganization during S-phase

Observed/Expected Hi-C matrices and corresponding PC1 compartment profiles for six genomic regions (listed below), comparing late G1 and early S phase. Purple arrowheads indicate loss of intra-A compartment signal in early S phase relative to late G1, while black arrowheads mark reduced contact frequency between neighboring A compartments. The right panel shows the differential contact heatmap (ES – LG1, early S – late G1). Region coordinates from top to bottom: chr1: 126–144 Mb; chr4: 38–51 Mb; chr5: 110–133 Mb; chr11: 71–81 Mb; chr15: 71–90 Mb; chr17: 22–38 Mb.

Figure S11. Correlation between reconstructed 3D structures and Hi-C data across the cell cycle

Absolute Spearman correlation coefficients between experimentally derived Hi-C contact matrices (200-kb bins) and distances from 3D genome structures reconstructed using the LorDG-3D Modeler in GenomeFlow[26] using a conversion factor of 0.6 (10,000 iterations). Line plots show correlations for all chromosomes across different cell-cycle phases.

Figure S12. Simulated 3D dynamics of A and B compartment domains across cell-cycle phases

(A) Comparison of mean bin-to-bin distances between A and B compartment domains (> 1 Mb) across cell-cycle phases. Boxplots show the median and quartiles. Each point represents a single domain. Pairwise comparisons between consecutive phases were performed using the Wilcoxon rank-sum test, and p-values were adjusted using the Benjamini-Hochberg method. **(B,C)** Mean bin-to-bin distances for A compartment domains **(B)** and B compartment domains **(C)** by chromosome. Data are presented as mean ± SD (points and error bars). Numbers indicate the total number of domains per chromosome. Data in panels **(A–C)** are from merged biological replicates (N=2) analyzed at 200-kb resolution.

Figure 1

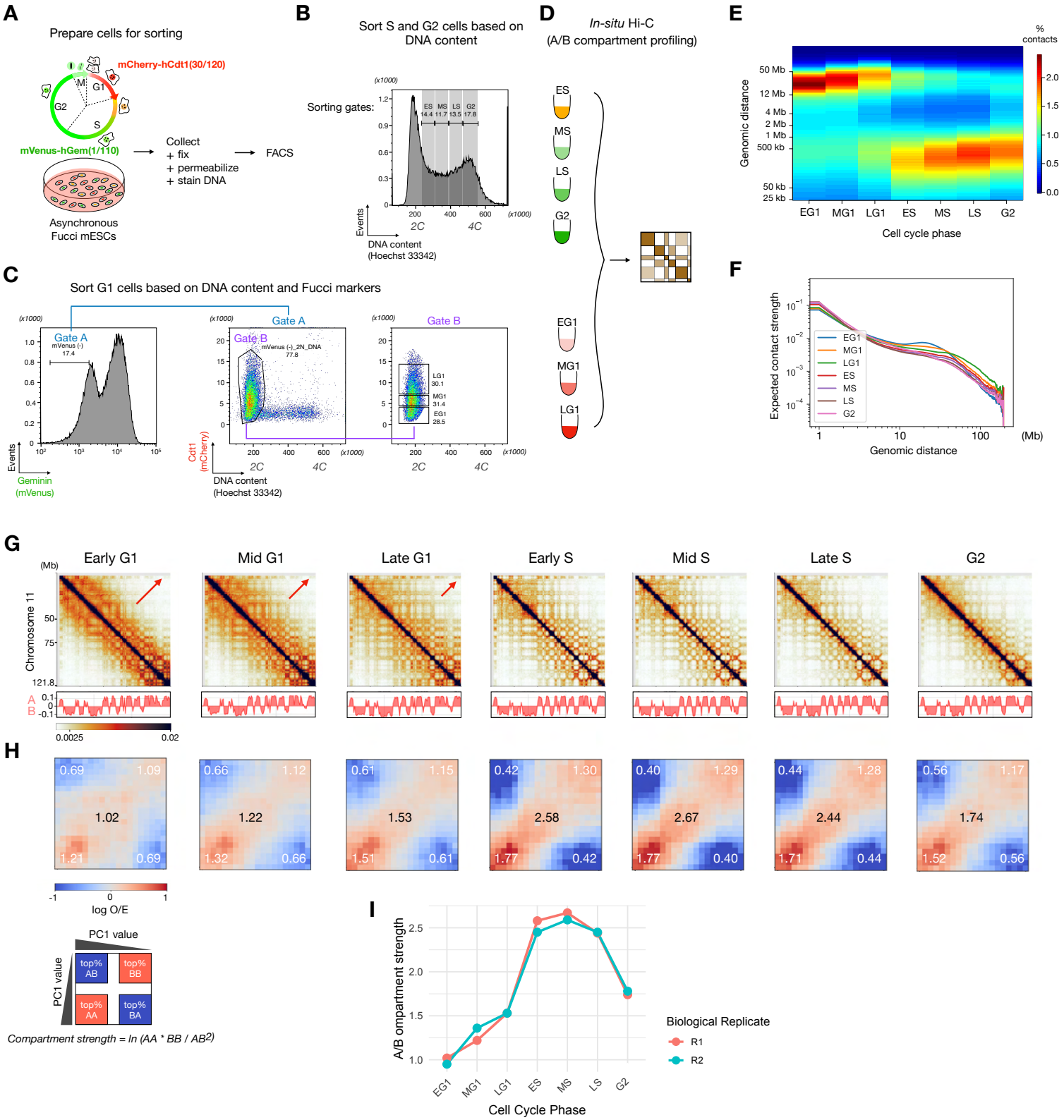
A
Prepare cells for sorting
mCherry-hCdt1(30/120)
mVenus-hGem(1/110)
M
G1
S
G2
Collect
+ fix
+ permeabilize
+ stain DNA
FACS
Asynchronous
Fucci mESCs
B
Sort S and G2 cells based on
DNA content
Sorting gates:
ES
MS
LS
G2
Events
DNA content
(Hoechst 33342)
2C
4C
C
Sort G1 cells based on DNA content and Fucci markers
Gate A
Gate B
Geminin
(mVenus)
Cdt1
(mCherry)
DNA content
(Hoechst 33342)
D
In-situ Hi-C
(A/B compartment profiling)
ES
MS
LS
G2
EG1
MG1
LG1
E
% contacts
Genomic distance
Cell cycle phase
F
Expected contact strength
Genomic distance
(Mb)
G
Early G1
Mid G1
Late G1
Early S
Mid S
Late S
G2
Chromosome 11
(Mb)
H
log O/E
PC1 value
top% AB
top% BB
top% AA
top% BA
Compartment strength = ln (AA * BB / AB2)
I
A/B compartment strength
Cell Cycle Phase
Biological Replicate
R1
R2

Figure 2

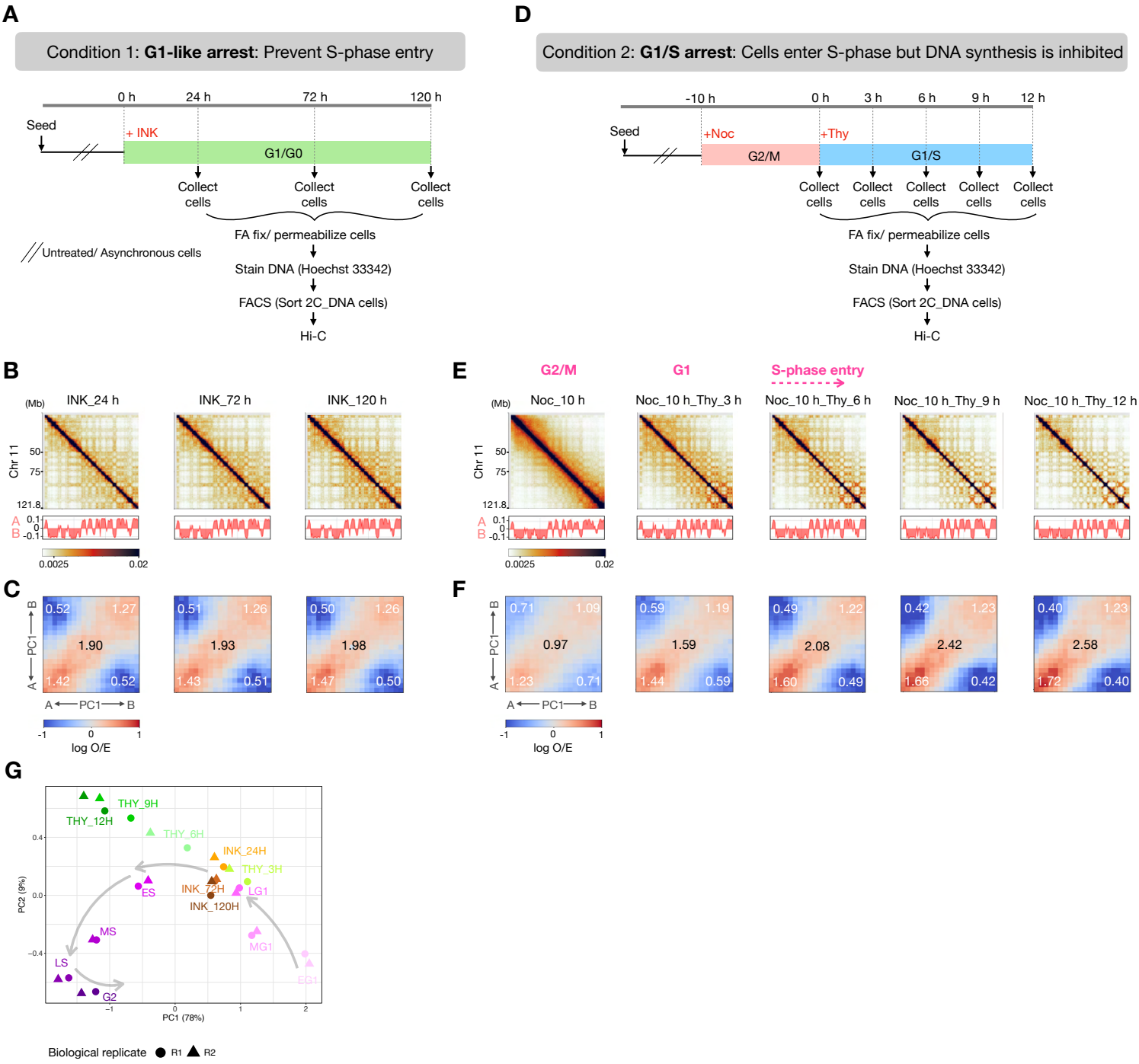
A
Condition 1: G1-like arrest: Prevent S-phase entry
0 h
24 h
72 h
120 h
Seed
+ INK
G1/G0
Collect cells
Collect cells
Collect cells
Untreated/ Asynchronous cells
FA fix/ permeabilize cells
Stain DNA (Hoechst 33342)
FACS (Sort 2C_DNA cells)
Hi-C
D
Condition 2: G1/S arrest: Cells enter S-phase but DNA synthesis is inhibited
-10 h
0 h
3 h
6 h
9 h
12 h
Seed
+Noc
+Thy
G2/M
G1/S
Collect cells
Collect cells
Collect cells
Collect cells
Collect cells
FA fix/ permeabilize cells
Stain DNA (Hoechst 33342)
FACS (Sort 2C_DNA cells)
Hi-C
B
INK_24 h
INK_72 h
INK_120 h
(Mb)
Chr 11
50
75
121.8
A
B
0.1
0
-0.1
0.0025
0.02
E
G2/M
G1
S-phase entry
Noc_10 h
Noc_10 h_Thy_3 h
Noc_10 h_Thy_6 h
Noc_10 h_Thy_9 h
Noc_10 h_Thy_12 h
C
PC1
A
B
0.52
1.27
1.90
1.42
0.52
0.51
1.26
1.93
1.43
0.51
0.50
1.26
1.98
1.47
0.50
-1
0
1
log O/E
F
0.71
1.09
0.97
1.23
0.71
0.59
1.19
1.59
1.44
0.59
0.49
1.22
2.08
1.60
0.49
0.42
1.23
2.42
1.66
0.42
0.40
1.23
2.58
1.72
0.40
G
THY_9H
THY_12H
THY_6H
INK_24H
THY_3H
ES
INK_72H
LG1
INK_120H
MS
MG1
LS
EG1
G2
PC2 (9%)
PC1 (78%)
0.4
0.0
−0.4
−1
0
1
2
Biological replicate
R1
R2

Figure 3

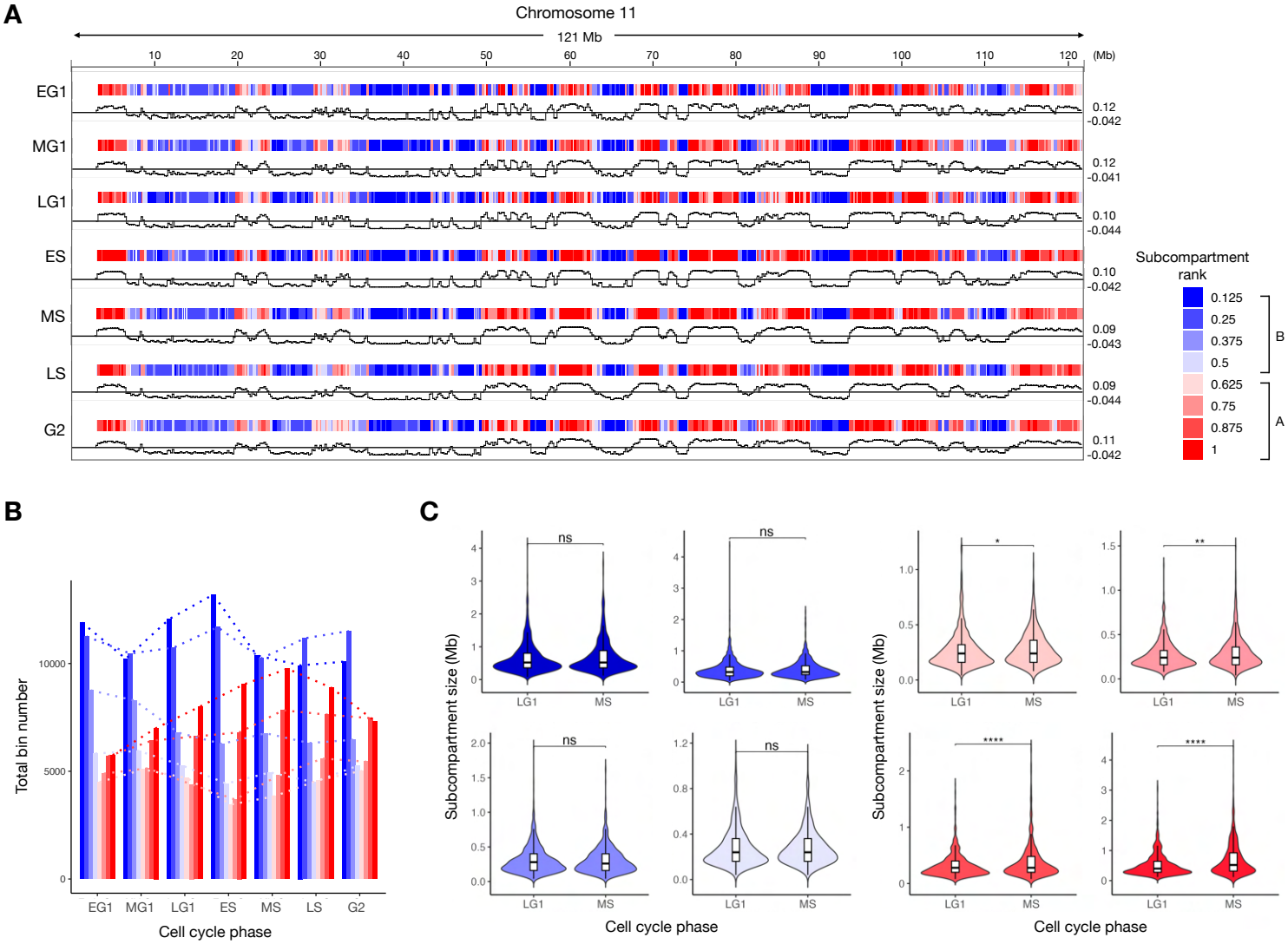
A
Chromosome 11
121 Mb
10
20
30
40
50
60
70
80
90
100
110
120
(Mb)
EG1
MG1
LG1
ES
MS
LS
G2
0.12
-0.042
0.12
-0.041
0.10
-0.044
0.10
-0.042
0.09
-0.043
0.09
-0.044
0.11
-0.042
Subcompartment rank
0.125
0.25
0.375
0.5
0.625
0.75
0.875
1
B
A
B
Total bin number
10000
5000
0
EG1
MG1
LG1
ES
MS
LS
G2
Cell cycle phase
C
Subcompartment size (Mb)
ns
*
**
****
LG1
MS
Cell cycle phase

Figure 4

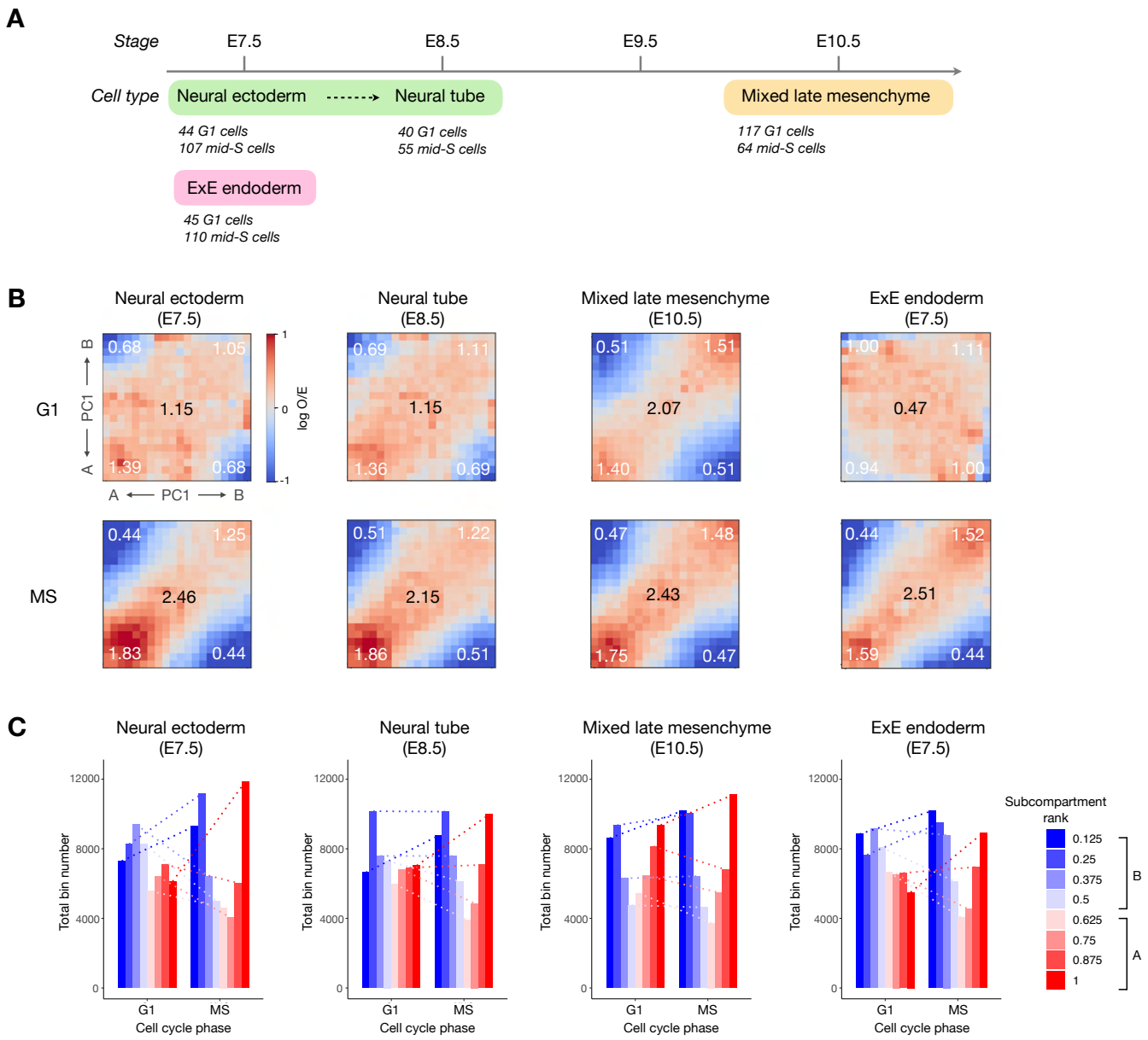
A
Stage
E7.5
E8.5
E9.5
E10.5
Cell type
Neural ectoderm
Neural tube
Mixed late mesenchyme
44 G1 cells
107 mid-S cells
40 G1 cells
55 mid-S cells
117 G1 cells
64 mid-S cells
ExE endoderm
45 G1 cells
110 mid-S cells
B
Neural ectoderm (E7.5)
Neural tube (E8.5)
Mixed late mesenchyme (E10.5)
ExE endoderm (E7.5)
G1
MS
A ← PC1 → B
log O/E
C
Total bin number
Cell cycle phase
Subcompartment rank
0.125
0.25
0.375
0.5
0.625
0.75
0.875
1
B
A

Figure 5

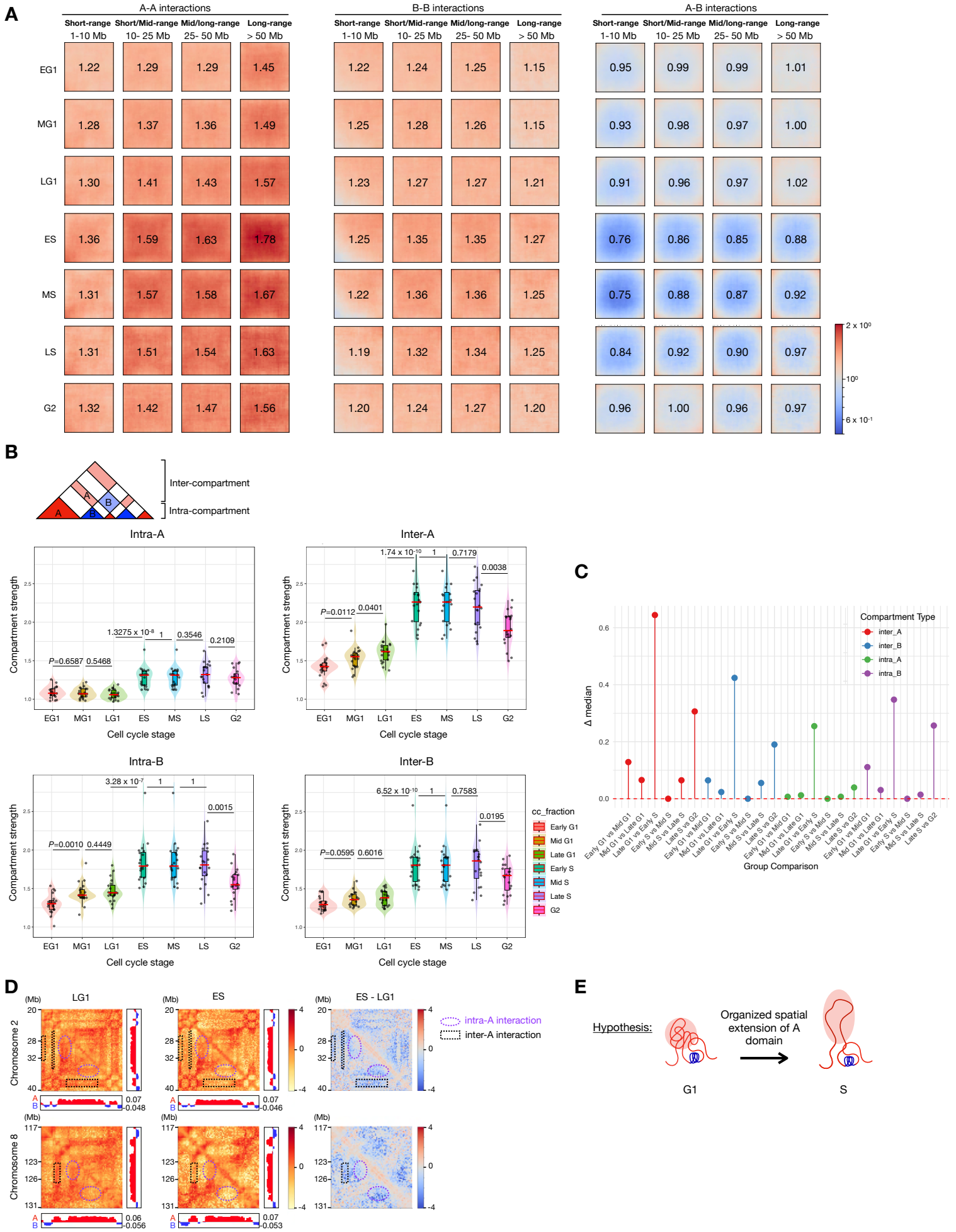

A
A-A interactions
B-B interactions
A-B interactions
Short-range 1-10 Mb
Short/Mid-range 10- 25 Mb
Mid/long-range 25- 50 Mb
Long-range > 50 Mb
EG1 1.22 1.29 1.29 1.45 1.22 1.24 1.25 1.15 0.95 0.99 0.99 1.01
MG1 1.28 1.37 1.36 1.49 1.25 1.28 1.26 1.15 0.93 0.98 0.97 1.00
LG1 1.30 1.41 1.43 1.57 1.23 1.27 1.27 1.21 0.91 0.96 0.97 1.02
ES 1.36 1.59 1.63 1.78 1.25 1.35 1.35 1.27 0.76 0.86 0.85 0.88
MS 1.31 1.57 1.58 1.67 1.22 1.36 1.36 1.25 0.75 0.88 0.87 0.92
LS 1.31 1.51 1.54 1.63 1.19 1.32 1.34 1.25 0.84 0.92 0.90 0.97
G2 1.32 1.42 1.47 1.56 1.20 1.24 1.27 1.20 0.96 1.00 0.96 0.97
2 x 10⁰
10⁰
6 x 10⁻¹
B
Inter-compartment
Intra-compartment
Intra-A
Inter-A
Intra-B
Inter-B
Compartment strength
Cell cycle stage
EG1 MG1 LG1 ES MS LS G2
P=0.6587 0.5468 1.3275 x 10⁻⁸ 1 0.3546 0.2109
P=0.0112 0.0401 1.74 x 10⁻¹⁰ 1 0.7179 0.0038
P=0.0010 0.4449 3.28 x 10⁻⁷ 1 1 0.0015
P=0.0595 0.6016 6.52 x 10⁻¹⁰ 1 0.7583 0.0195
cc_fraction
Early G1
Mid G1
Late G1
Early S
Mid S
Late S
G2
C
Compartment Type
inter_A
inter_B
intra_A
intra_B
Δ median
Group Comparison
D
LG1
ES
ES - LG1
Chromosome 2
Chromosome 8
(Mb)
intra-A interaction
inter-A interaction
E
Hypothesis:
Organized spatial extension of A domain
G1
S

Figure 6

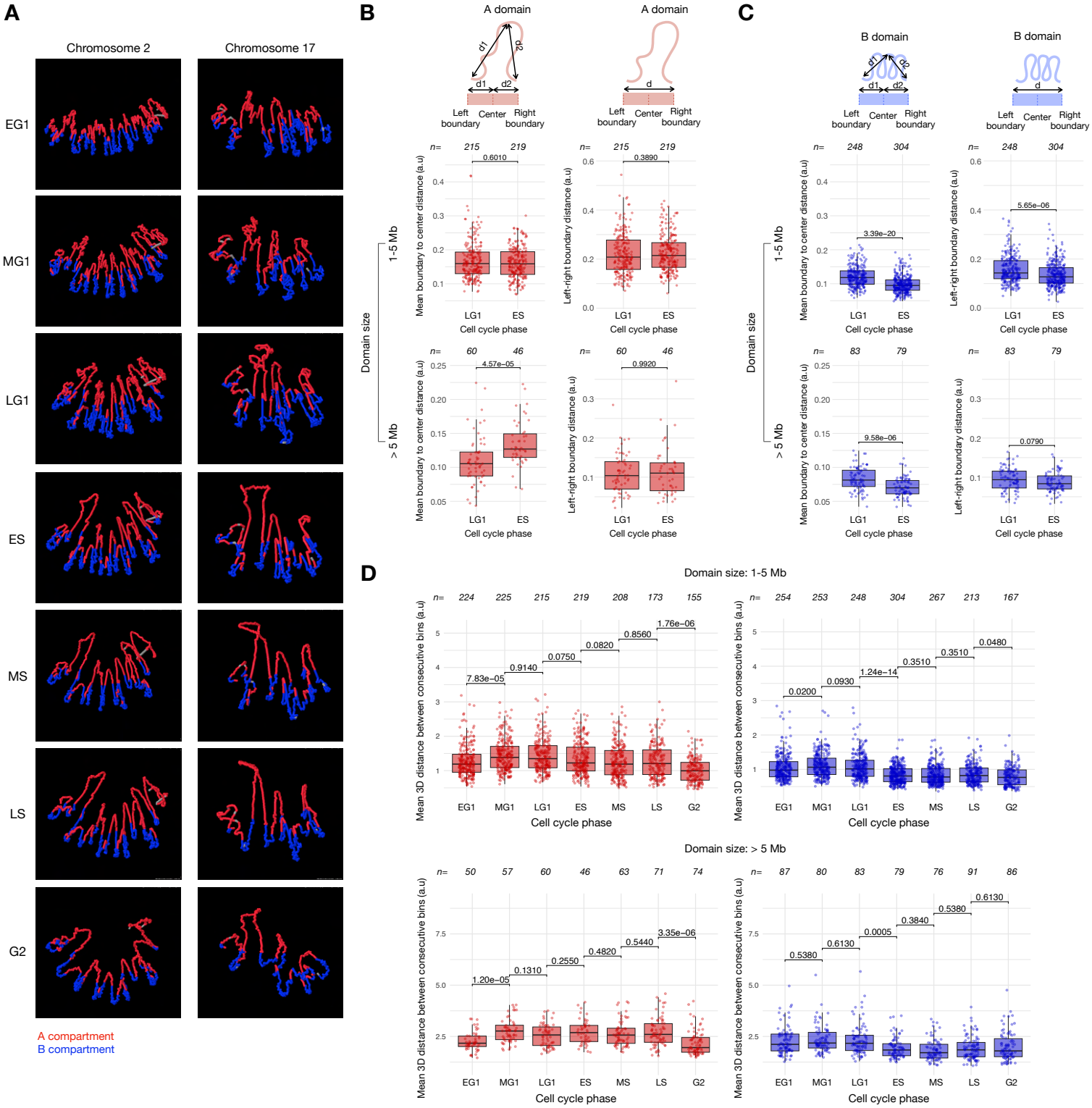
A
Chromosome 2
Chromosome 17
EG1
MG1
LG1
ES
MS
LS
G2
A compartment
B compartment
B
A domain
A domain
d1
d2
d
Left boundary
Center
Right boundary
Domain size
1-5 Mb
> 5 Mb
Mean boundary to center distance (a.u)
Left-right boundary distance (a.u)
Cell cycle phase
LG1
ES
n= 215 219
0.6010
0.3890
n= 60 46
4.57e−05
0.9920
C
B domain
B domain
n= 248 304
3.39e−20
5.65e−06
n= 83 79
9.58e−06
0.0790
D
Domain size: 1-5 Mb
Mean 3D distance between consecutive bins (a.u)
n= 224 225 215 219 208 173 155
7.83e−05
0.9140
0.0750
0.0820
0.8560
1.76e−06
n= 254 253 248 304 267 213 167
0.0200
0.0930
1.24e−14
0.3510
0.3510
0.0480
EG1
MG1
LG1
ES
MS
LS
G2
Domain size: > 5 Mb
n= 50 57 60 46 63 71 74
1.20e−05
0.1310
0.2550
0.4820
0.5440
3.35e−06
n= 87 80 83 79 76 91 86
0.5380
0.6130
0.0005
0.3840
0.5380
0.6130

Figure 7

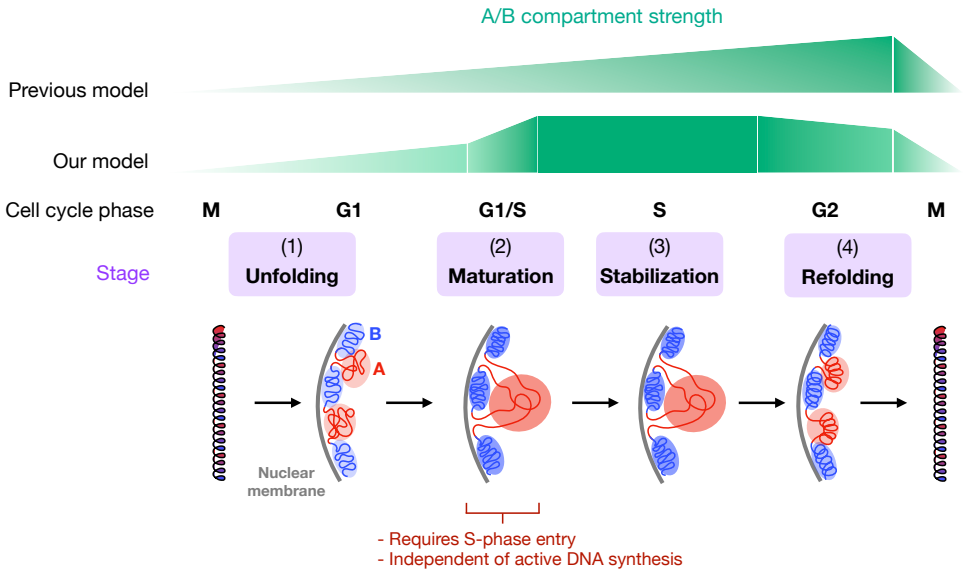
A/B compartment strength
Previous model
Our model
Cell cycle phase
M
G1
G1/S
S
G2
M
Stage
(1)
Unfolding
(2)
Maturation
(3)
Stabilization
(4)
Refolding
B
A
Nuclear membrane
- Requires S-phase entry
- Independent of active DNA synthesis

Figure S1

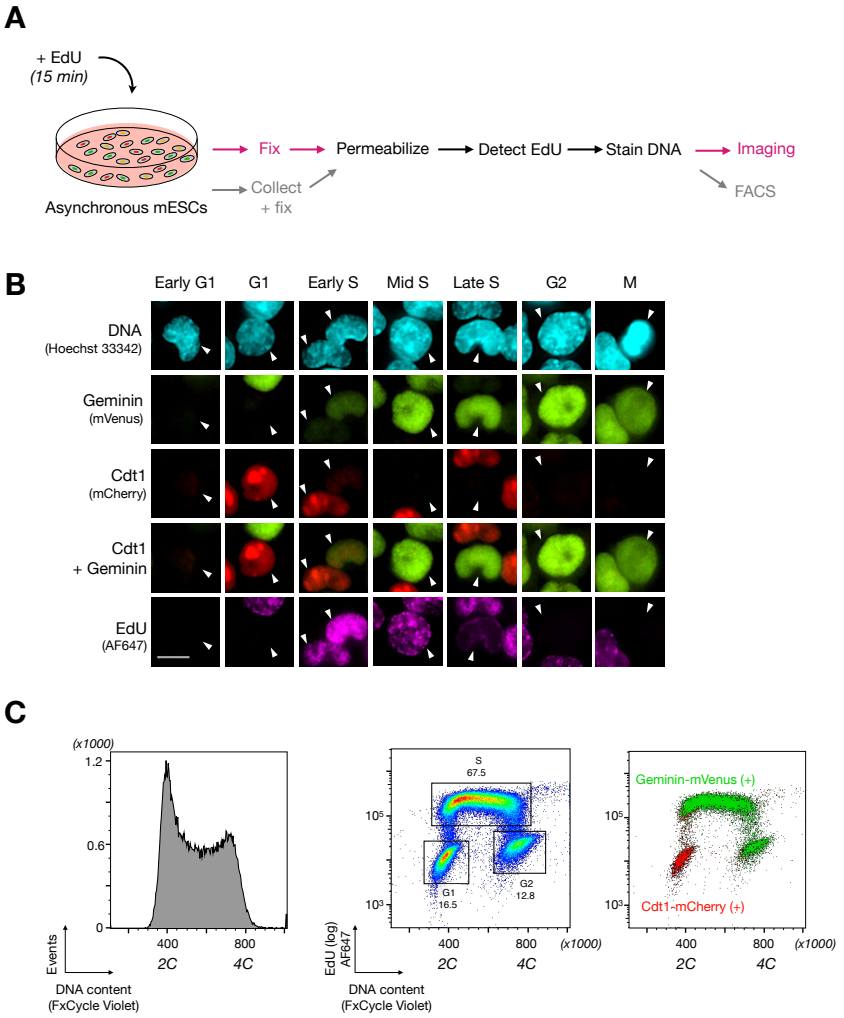
A
+ EdU
(15 min)
Asynchronous mESCs
Fix
Collect
+ fix
Permeabilize
Detect EdU
Stain DNA
Imaging
FACS
B
Early G1
G1
Early S
Mid S
Late S
G2
M
DNA
(Hoechst 33342)
Geminin
(mVenus)
Cdt1
(mCherry)
Cdt1
+ Geminin
EdU
(AF647)
C
(x1000)
1.2
0.6
0
Events
400
800
2C
4C
DNA content
(FxCycle Violet)
S
67.5
G1
16.5
G2
12.8
EdU (log)
AF647
(x1000)
Geminin-mVenus (+)
Cdt1-mCherry (+)

Figure S2

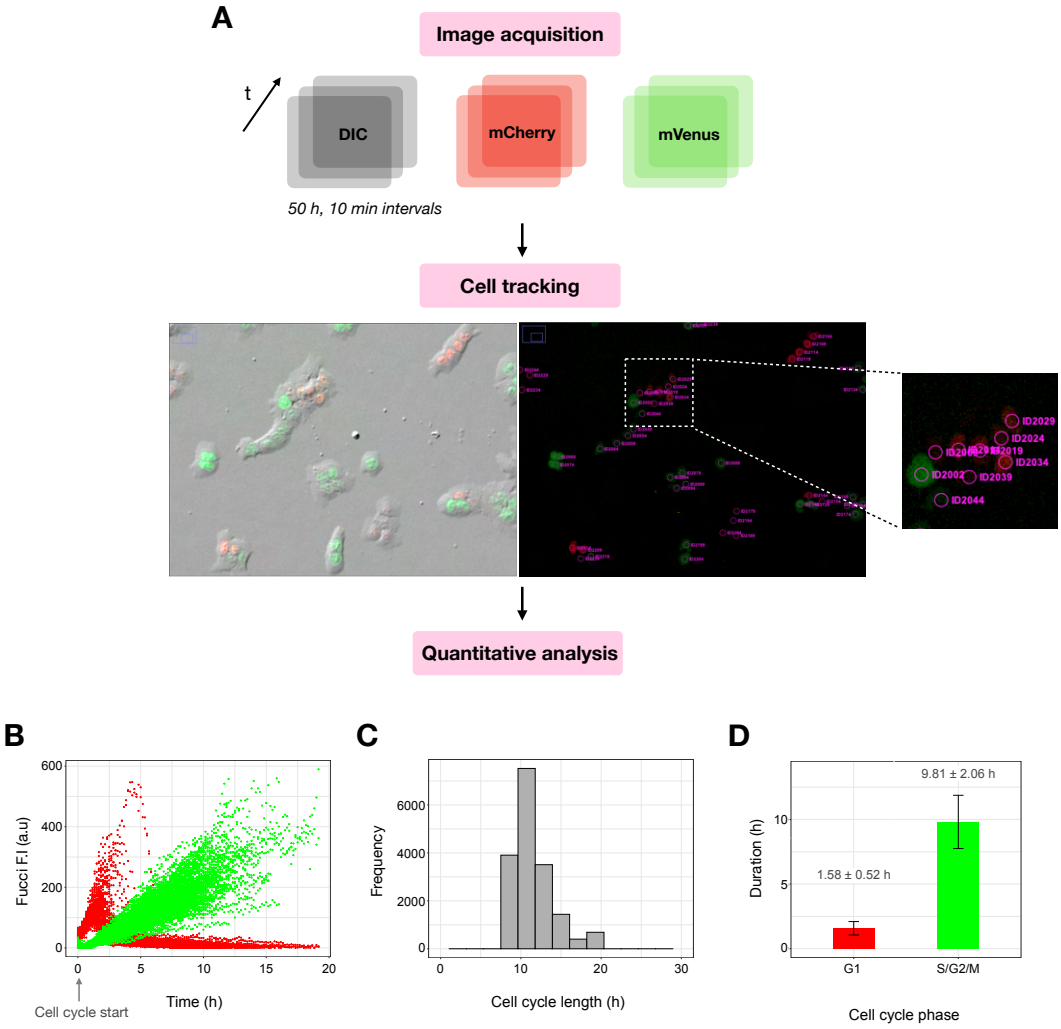
A
Image acquisition
t
DIC
mCherry
mVenus
50 h, 10 min intervals
Cell tracking
ID2029
ID2024
ID2019
ID2034
ID2002
ID2039
ID2044
Quantitative analysis
B
Fucci F.I (a.u)
600
400
200
0
0
5
10
15
20
Time (h)
Cell cycle start
C
Frequency
6000
4000
2000
0
0
10
20
30
Cell cycle length (h)
D
Duration (h)
10
5
0
9.81 ± 2.06 h
1.58 ± 0.52 h
G1
S/G2/M
Cell cycle phase

Figure S3

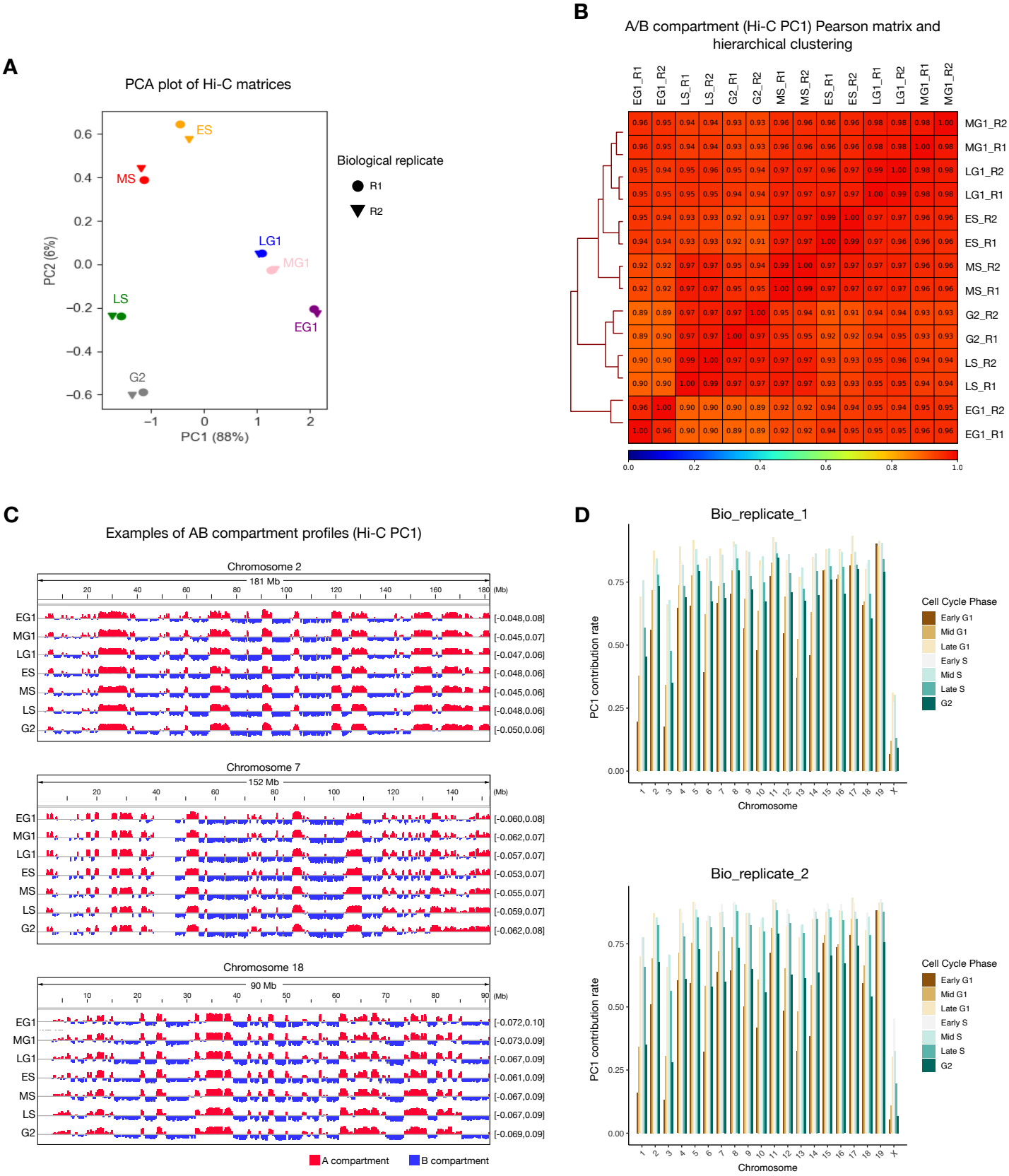
A
PCA plot of Hi-C matrices
ES
MS
LG1
MG1
LS
EG1
G2
PC2 (6%)
PC1 (88%)
Biological replicate
R1
R2
B
A/B compartment (Hi-C PC1) Pearson matrix and hierarchical clustering
EG1_R1
EG1_R2
LS_R1
LS_R2
G2_R1
G2_R2
MS_R1
MS_R2
ES_R1
ES_R2
LG1_R1
LG1_R2
MG1_R1
MG1_R2
C
Examples of AB compartment profiles (Hi-C PC1)
Chromosome 2
181 Mb
Chromosome 7
152 Mb
Chromosome 18
90 Mb
EG1
MG1
LG1
ES
MS
LS
G2
A compartment
B compartment
D
Bio_replicate_1
Bio_replicate_2
PC1 contribution rate
Chromosome
Cell Cycle Phase
Early G1
Mid G1
Late G1
Early S
Mid S
Late S
G2

Figure S4

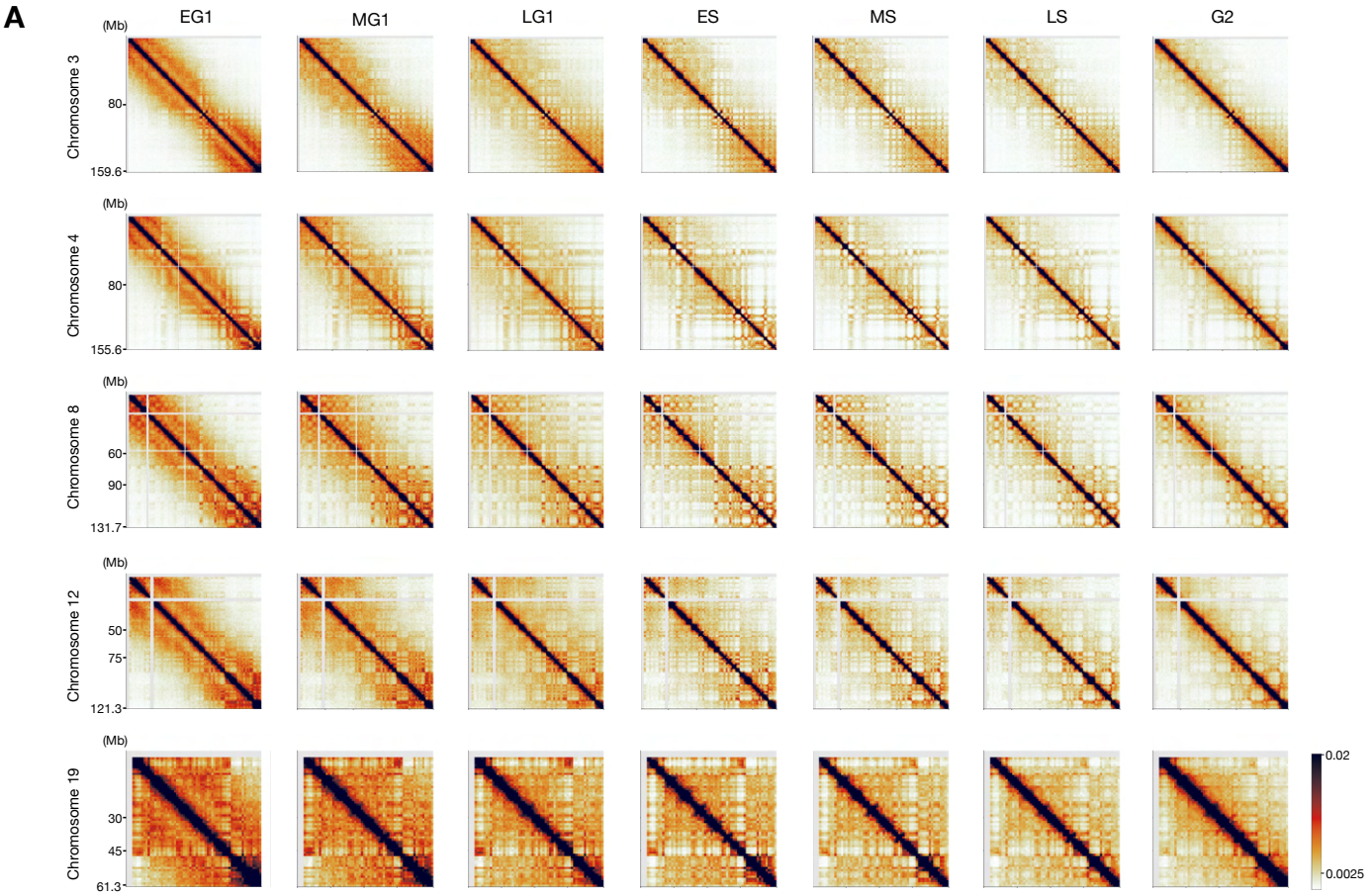
A
EG1
MG1
LG1
ES
MS
LS
G2
Chromosome 3
Chromosome 4
Chromosome 8
Chromosome 12
Chromosome 19
(Mb)
0.02
0.0025

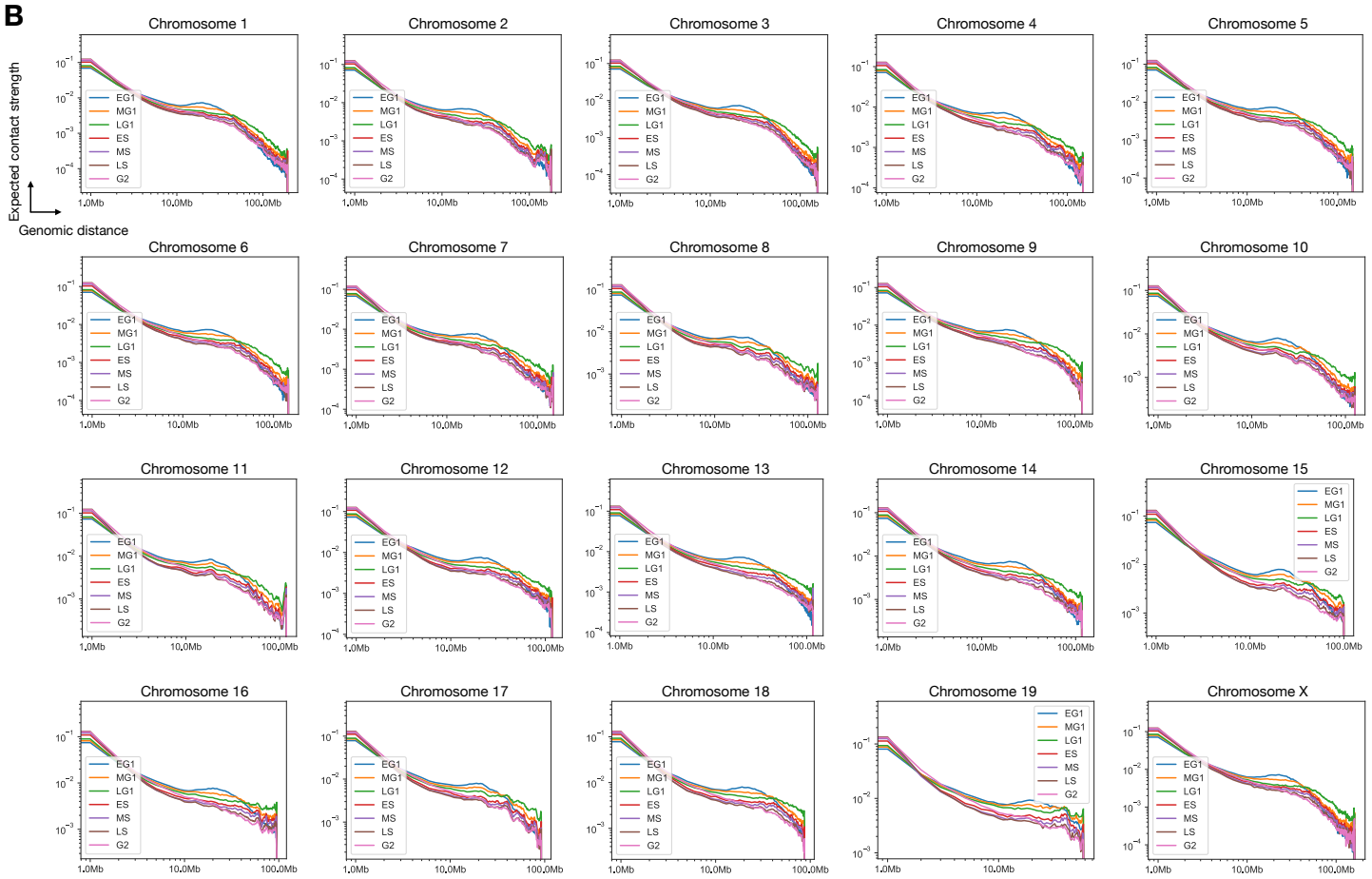
B
Expected contact strength
Genomic distance
Chromosome 1
Chromosome 2
Chromosome 3
Chromosome 4
Chromosome 5
Chromosome 6
Chromosome 7
Chromosome 8
Chromosome 9
Chromosome 10
Chromosome 11
Chromosome 12
Chromosome 13
Chromosome 14
Chromosome 15
Chromosome 16
Chromosome 17
Chromosome 18
Chromosome 19
Chromosome X
EG1
MG1
LG1
ES
MS
LS
G2
1.0Mb
10.0Mb
100.0Mb

Figure S5

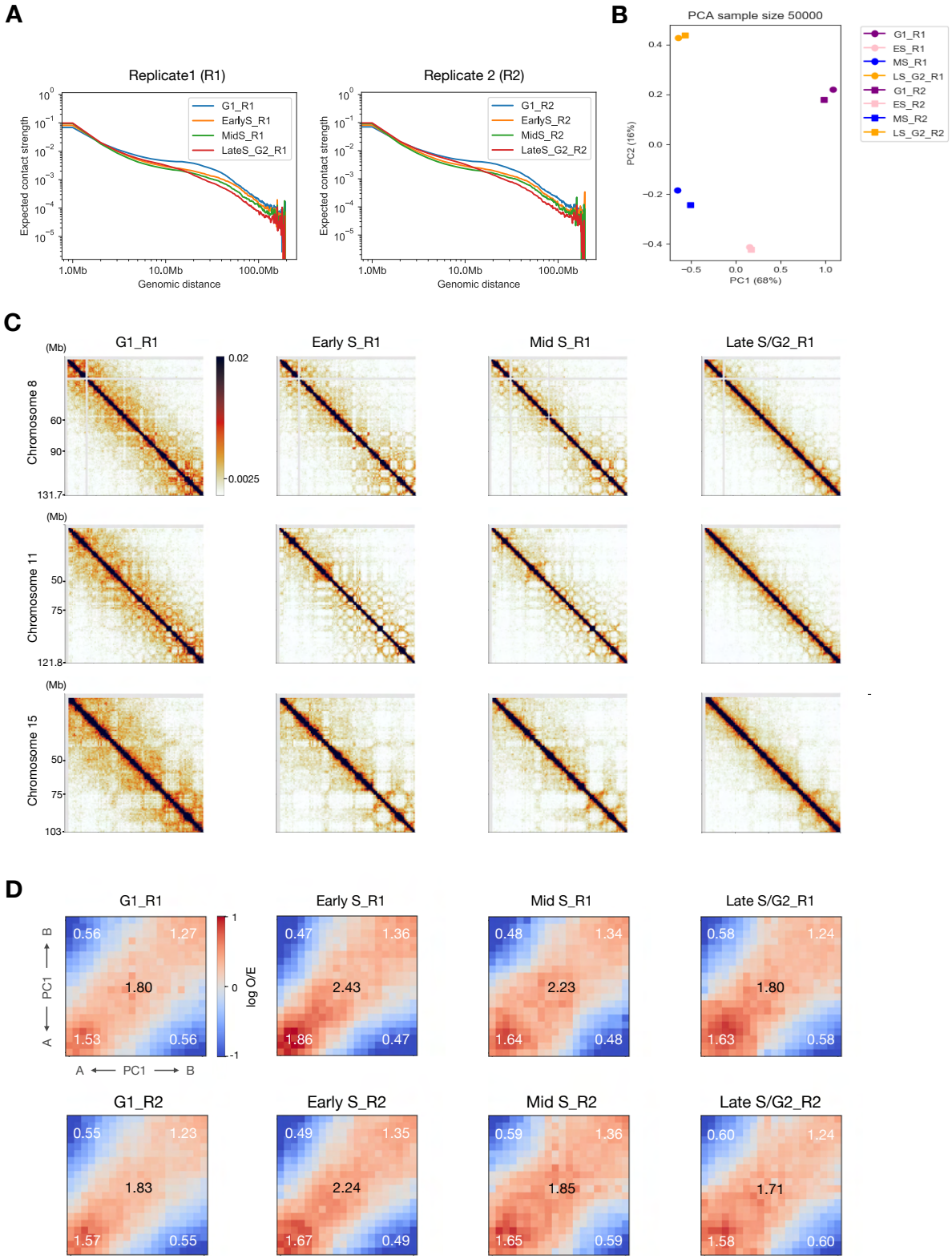
A
Replicate1 (R1)
Replicate 2 (R2)
Expected contact strength
Genomic distance
1.0Mb
10.0Mb
100.0Mb
G1_R1
EarlyS_R1
MidS_R1
LateS_G2_R1
G1_R2
EarlyS_R2
MidS_R2
LateS_G2_R2
B
PCA sample size 50000
PC1 (68%)
PC2 (16%)
G1_R1
ES_R1
MS_R1
LS_G2_R1
G1_R2
ES_R2
MS_R2
LS_G2_R2
C
G1_R1
Early S_R1
Mid S_R1
Late S/G2_R1
Chromosome 8
Chromosome 11
Chromosome 15
(Mb)
0.02
0.0025
D
G1_R1
Early S_R1
Mid S_R1
Late S/G2_R1
G1_R2
Early S_R2
Mid S_R2
Late S/G2_R2
A ⟵ PC1 ⟶ B
log O/E
0.56
1.27
1.80
1.53
0.56
0.47
1.36
2.43
1.86
0.47
0.48
1.34
2.23
1.64
0.48
0.58
1.24
1.80
1.63
0.58
0.55
1.23
1.83
1.57
0.55
0.49
1.35
2.24
1.67
0.49
0.59
1.36
1.85
1.65
0.59
0.60
1.24
1.71
1.58
0.60

Figure S6

A

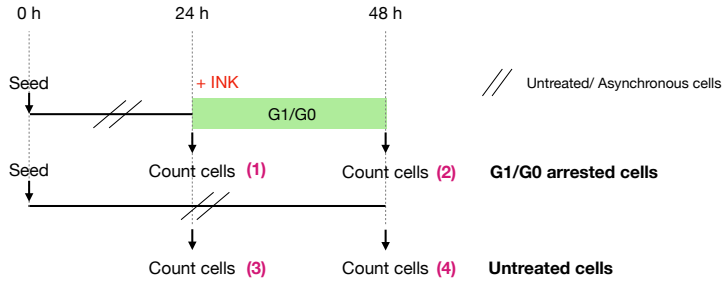

B

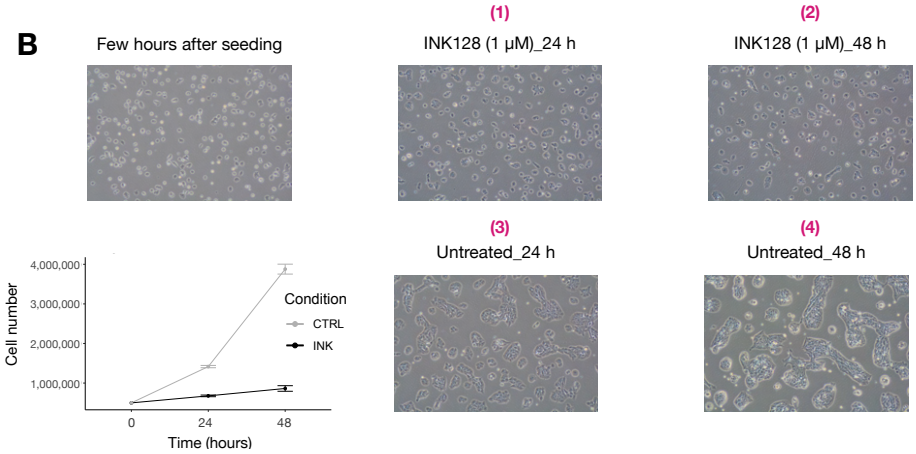

C

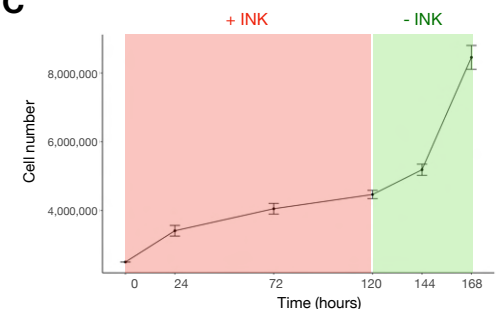

Figure S7

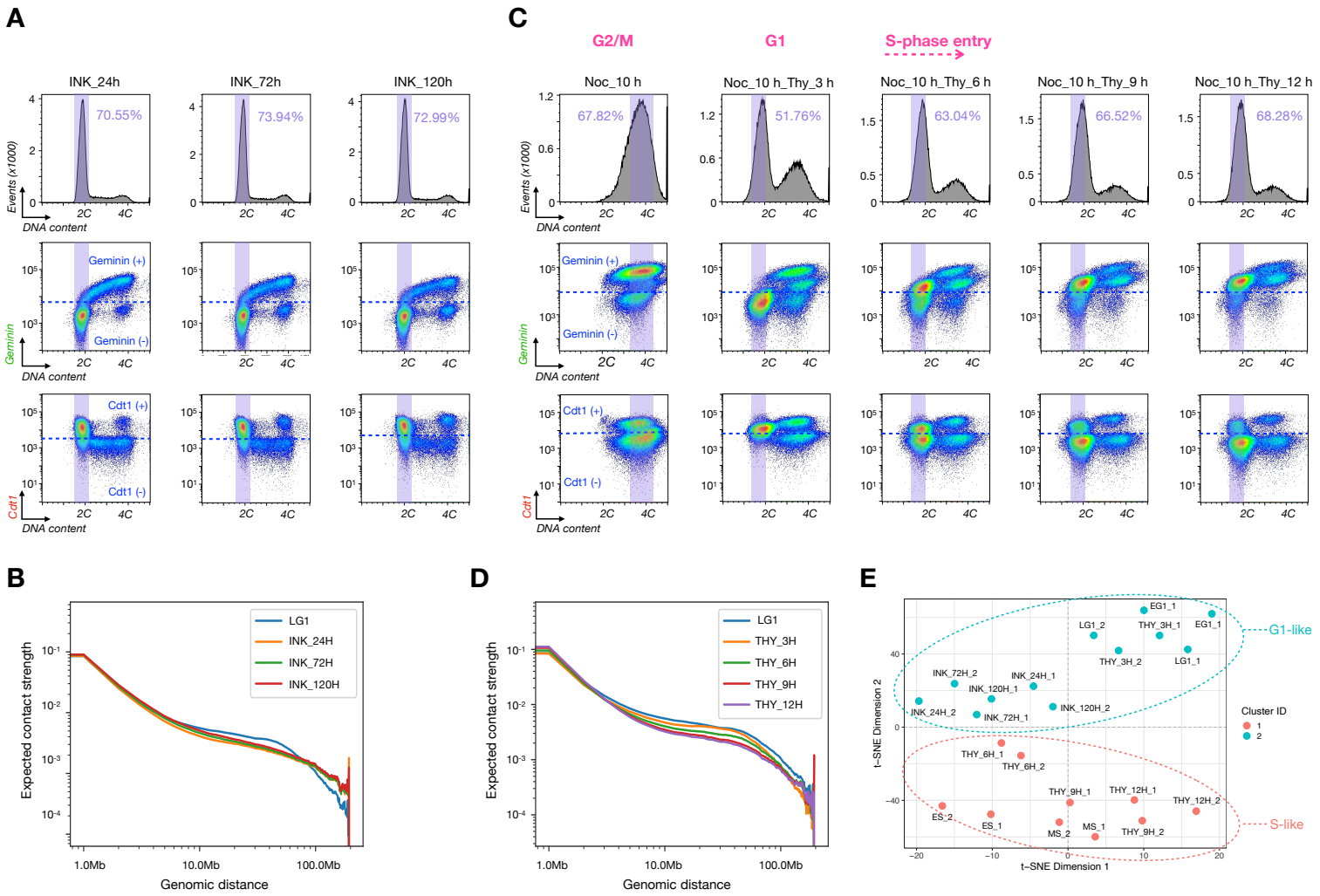
A
INK_24h
INK_72h
INK_120h
70.55%
73.94%
72.99%
Events (x1000)
DNA content
Geminin (+)
Geminin (-)
Geminin
Cdt1 (+)
Cdt1 (-)
Cdt1
C
G2/M
G1
S-phase entry
Noc_10 h
Noc_10 h_Thy_3 h
Noc_10 h_Thy_6 h
Noc_10 h_Thy_9 h
Noc_10 h_Thy_12 h
67.82%
51.76%
63.04%
66.52%
68.28%
B
Expected contact strength
Genomic distance
LG1
INK_24H
INK_72H
INK_120H
D
THY_3H
THY_6H
THY_9H
THY_12H
E
t-SNE Dimension 1
t-SNE Dimension 2
G1-like
S-like
Cluster ID
EG1_1
LG1_2
THY_3H_1
LG1_1
THY_3H_2
INK_72H_2
INK_24H_1
INK_120H_1
INK_120H_2
INK_24H_2
INK_72H_1
THY_6H_1
THY_6H_2
THY_9H_1
THY_12H_1
THY_12H_2
ES_2
ES_1
MS_2
MS_1
THY_9H_2

Figure S8

Chromosome 2
181 Mb
20
40
60
80
100
120
140
160
180
(Mb)
Subcompartment rank
0.125
0.25
0.375
0.5
0.625
0.75
0.875
1
B
A
EG1
MG1
LG1
ES
MS
LS
G2
[-0.048,0.08]
[-0.045,0.07]
[-0.047,0.06]
[-0.048,0.06]
[-0.045,0.06]
[-0.048,0.06]
[-0.050,0.06]
Chromosome 6
149 Mb
20
40
60
80
100
120
140
(Mb)
EG1
MG1
LG1
ES
MS
LS
G2
[-0.056,0.10]
[-0.052,0.08]
[-0.053,0.07]
[-0.048,0.07]
[-0.050,0.07]
[-0.050,0.07]
[-0.049,0.08]
Chromosome 13
120 Mb
20
40
60
80
100
120
(Mb)
EG1
MG1
LG1
ES
MS
LS
G2
[-0.075,0.10]
[-0.067,0.09]
[-0.067,0.08]
[-0.061,0.08]
[-0.059,0.08]
[-0.062,0.08]
[-0.063,0.08]
Chromosome 15
103 Mb
20
40
60
80
100
(Mb)
EG1
MG1
LG1
ES
MS
LS
G2
[-0.065,0.08]
[-0.062,0.08]
[-0.061,0.08]
[-0.060,0.07]
[-0.060,0.07]
[-0.060,0.07]
[-0.066,0.08]

Figure S9

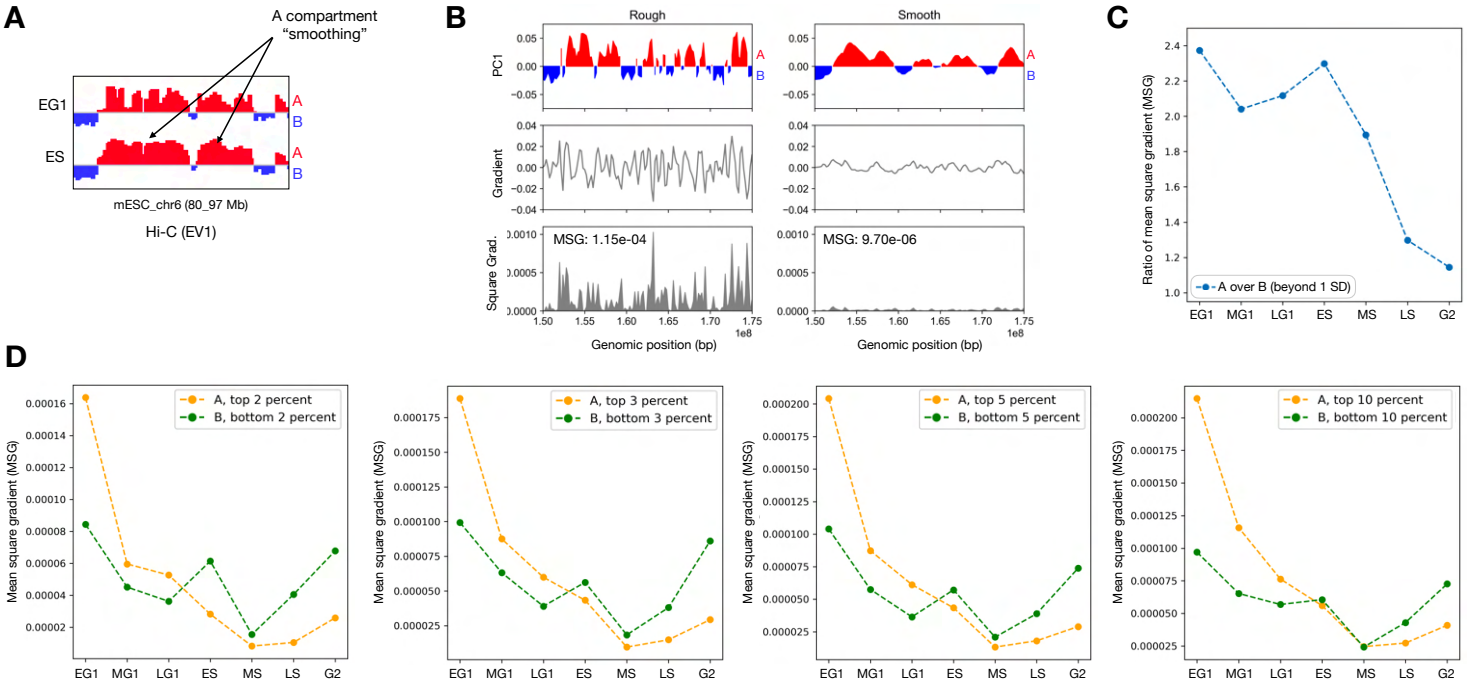
A
A compartment
"smoothing"
EG1
ES
A
B
mESC_chr6 (80_97 Mb)
Hi-C (EV1)
B
Rough
Smooth
PC1
Gradient
Square Grad.
MSG: 1.15e-04
MSG: 9.70e-06
Genomic position (bp)
1e8
C
Ratio of mean square gradient (MSG)
A over B (beyond 1 SD)
EG1 MG1 LG1 ES MS LS G2
D
Mean square gradient (MSG)
A, top 2 percent
B, bottom 2 percent
A, top 3 percent
B, bottom 3 percent
A, top 5 percent
B, bottom 5 percent
A, top 10 percent
B, bottom 10 percent

Figure S10

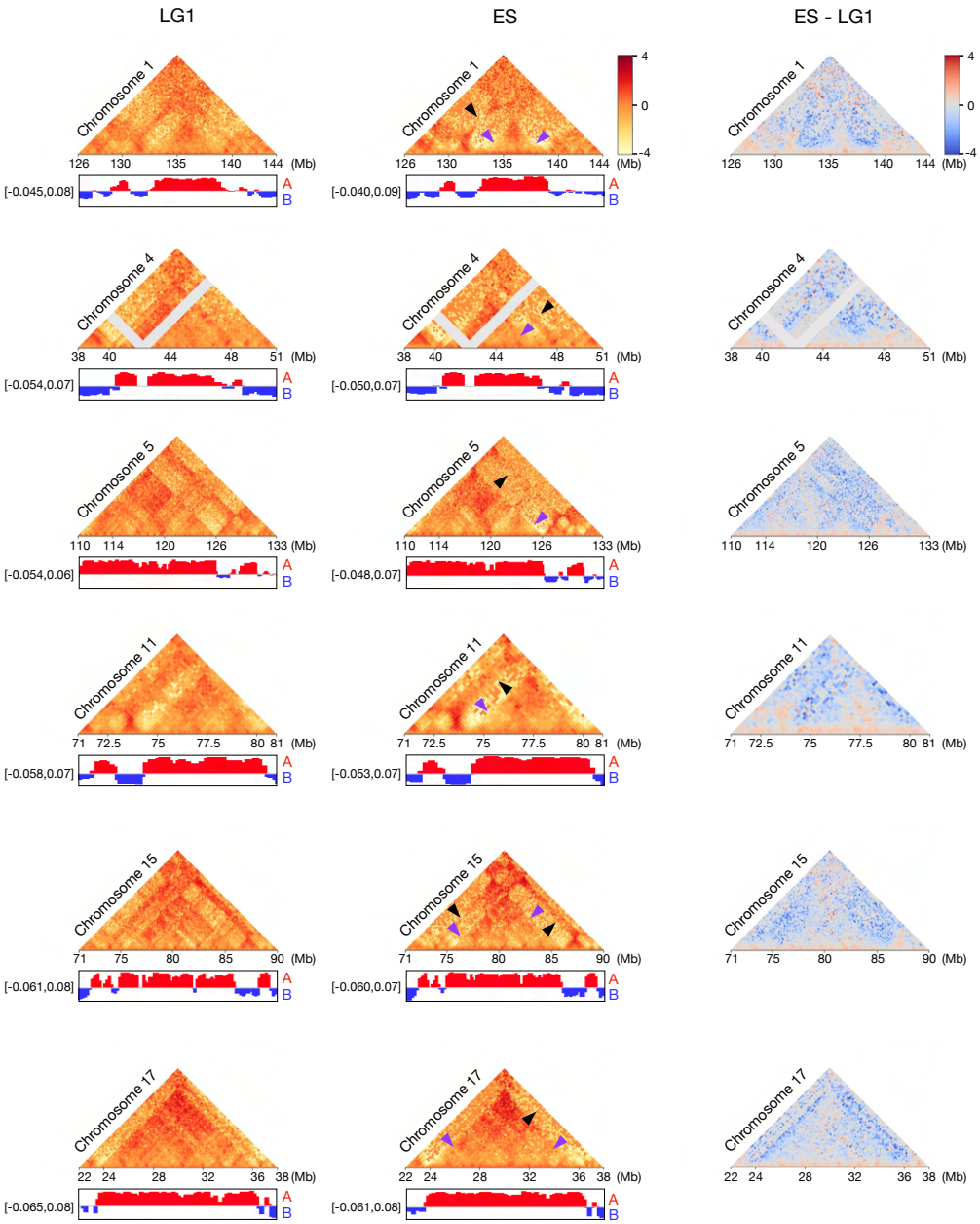
LG1
ES
ES - LG1
Chromosome 1
126 130 135 140 144 (Mb)
[-0.045,0.08]
[-0.040,0.09]
Chromosome 4
38 40 44 48 51 (Mb)
[-0.054,0.07]
[-0.050,0.07]
Chromosome 5
110 114 120 126 133 (Mb)
[-0.054,0.06]
[-0.048,0.07]
Chromosome 11
71 72.5 75 77.5 80 81 (Mb)
[-0.058,0.07]
[-0.053,0.07]
Chromosome 15
71 75 80 85 90 (Mb)
[-0.061,0.08]
[-0.060,0.07]
Chromosome 17
22 24 28 32 36 38 (Mb)
[-0.065,0.08]
[-0.061,0.08]
A
B
4
0
-4

Figure S11

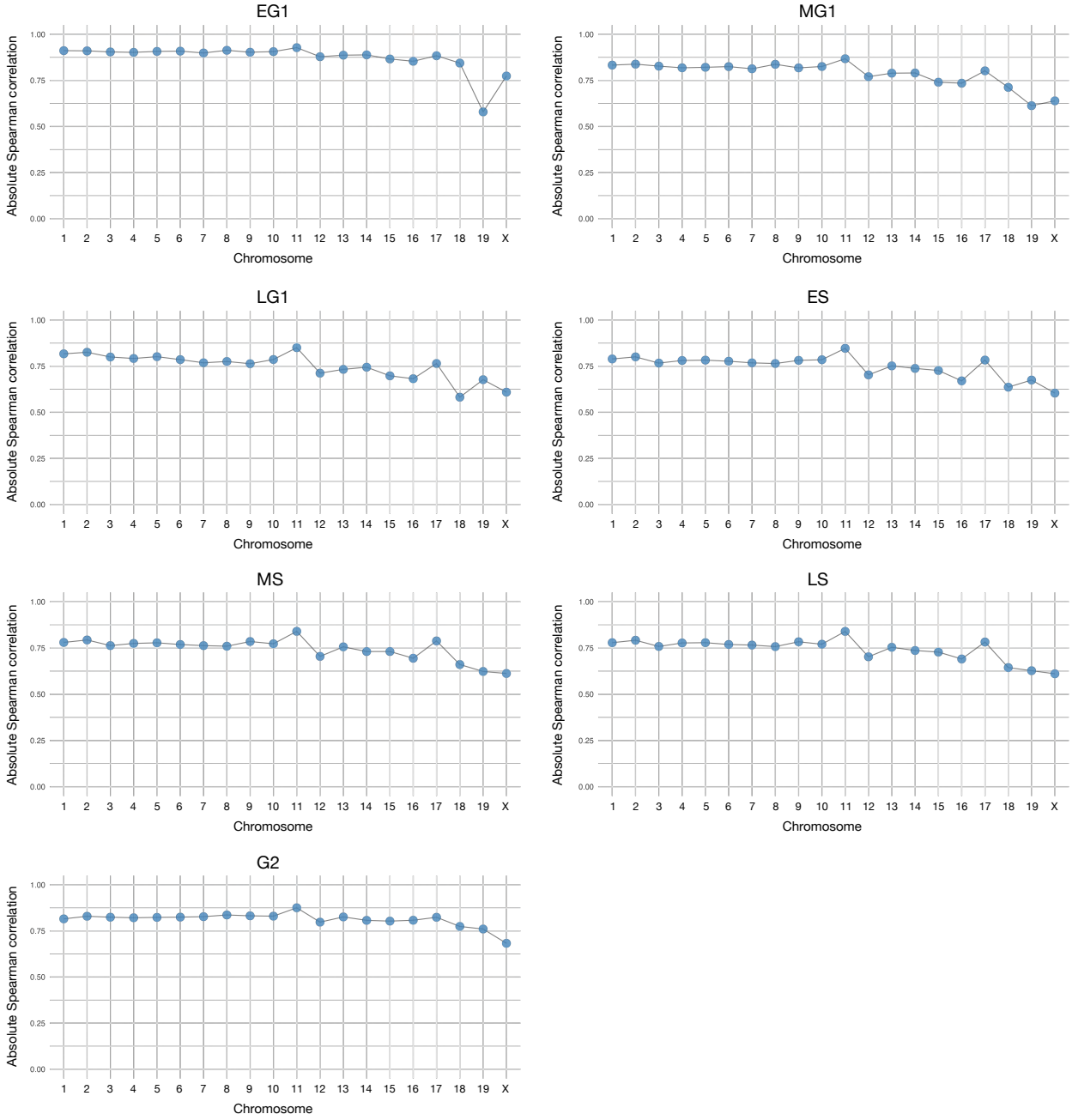
EG1
MG1
LG1
ES
MS
LS
G2
Absolute Spearman correlation
1.00
0.75
0.50
0.25
0.00
1 2 3 4 5 6 7 8 9 10 11 12 13 14 15 16 17 18 19 X
Chromosome

Figure S12

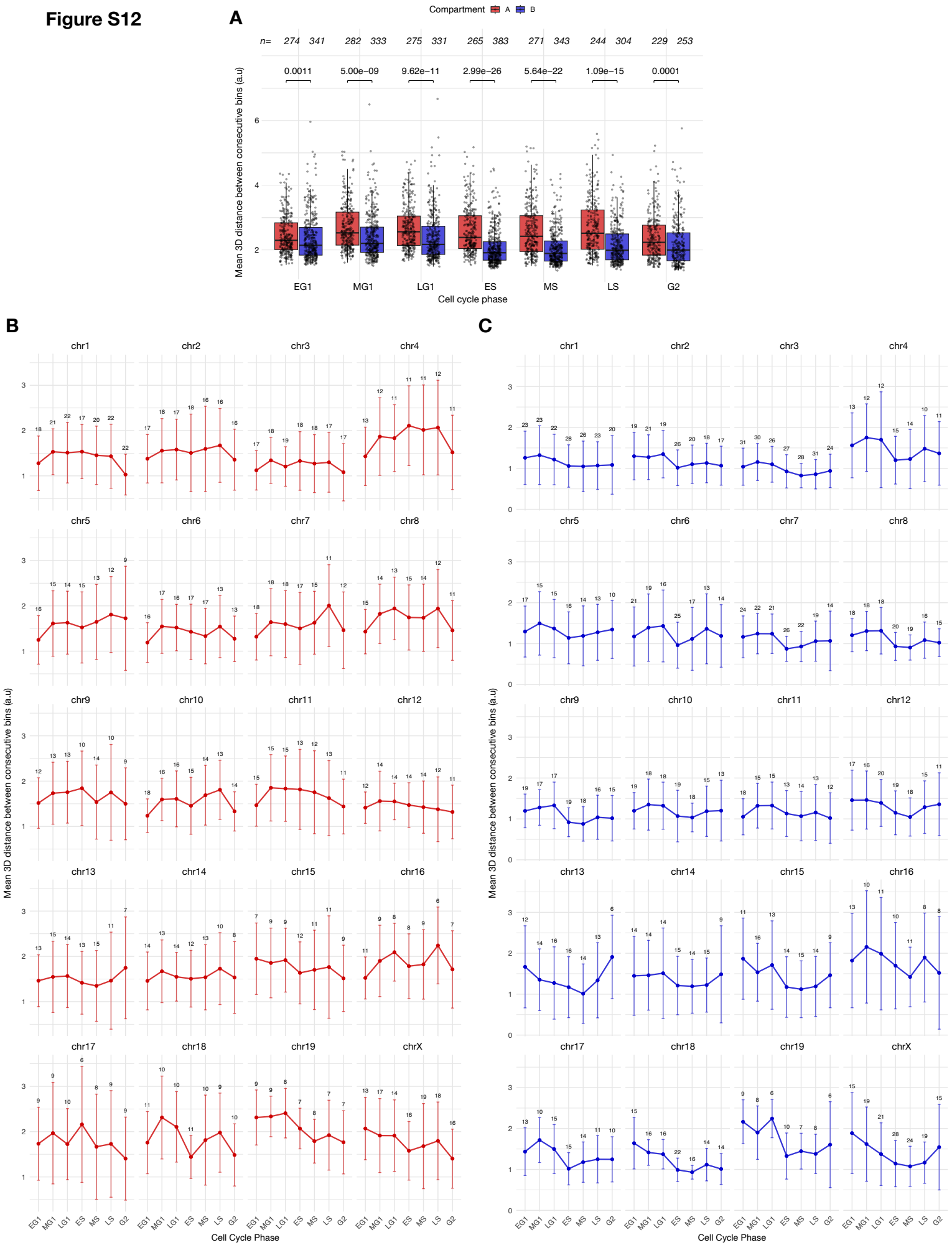
A
Compartment A B
n= 274 341 282 333 275 331 265 383 271 343 244 304 229 253
0.0011 5.00e−09 9.62e−11 2.99e−26 5.64e−22 1.09e−15 0.0001
Mean 3D distance between consecutive bins (a.u)
EG1 MG1 LG1 ES MS LS G2
Cell cycle phase
B
C
chr1 chr2 chr3 chr4 chr5 chr6 chr7 chr8 chr9 chr10 chr11 chr12 chr13 chr14 chr15 chr16 chr17 chr18 chr19 chrX
Mean 3D distance between consecutive bins (a.u)
Cell Cycle Phase